SLAC – PUB – 4563
March 1988
(T/E)

Prospects for Physics at e^+e^- Linear Colliders*

Gary J. Feldman
Stanford Linear Accelerator Center
Stanford University, Stanford, California 94309

1. Introduction

About a year ago, Burton Richter established two committees at SLAC to begin work on a proposal for a high-energy linear e^+e^- collider. One group, the Collider Accelerator Coordinating Committee, was charged with coordinating the study of accelerator issues and with coordinating the necessary accelerator research and development work. The other committee, the Collider Physics Coordinating Committee, was charged with studying the physics potential of such a collider and with making recommendations concerning the parameters that it should have. The members of these committees are listed in Table 1. The Accelerator Committee stayed small, acting as a true coordinating committee. The Physics Committee, on the other hand, grew throughout the year by exercising the option given to it by its charter to co-opt additional members.

These three lectures and the two lectures by Mike Peskin[1] will report on some of the work that has been done by these two committees. However, these reports should be considered unofficial and preliminary since neither committee has yet issued a report. All the conclusions that I draw in these lectures are my own and may differ from the conclusions the committees subsequently draw in their reports. Similarly, I have made numerous calculations in these lectures; any errors I have made are entirely my own.

* Work supported by the Department of Energy contract DE–AC03–76SF00515.

Presented at the SLAC Summer Institute on Particle Physics, Stanford, CA, August 10-21, 1987

Table 1: Collider Committee Memberships

Collider Physics Coordinating Committee	Collider Accelerator Coordinating Committee
Changrim Ahn	Tom Himel (Physics liaison)
Charles Baltay	Bob Palmer
Tim Barklow	Ewan Paterson (chairman)
Pat Burchat	John Rees
David Burke	Ron Ruth
Adrian Cooper	Rae Stiening
Claudio Dib	Perry Wilson
Gary Feldman	
Jack Gunion	
Howard Haber	
Tom Himel	
Sachio Komamiya	
Bryan Lynn	
Michael Peskin (chairman)	
Alfred Petersen	
John Rees (Accelerator liaison)	
Rick Van Kooten	

In Section 2, I will briefly review the present thinking on high-energy e^+e^- linear colliders, stressing those points that have consequences for detector design and physics analyses. Section 3 will discuss detector requirements. Sections 4 through 9 will discuss experimental aspects of the physics that can be done at these colliders: first the general physics environment, then a standard process, W^+W^- detection, and finally four examples of the discovery potential of these colliders — heavy quarks, heavy leptons, standard Higgs bosons, and charged Higgs bosons. These topics will constitute only a fraction of those that were studied by the Physics Committee. The conclusions of this study will be stated in Section 10.

2. Linear Collider Parameters and Experimental Consequences

2.1. Why Linear Colliders?

The first question we have to ask is why we want to consider linear colliders as opposed to storage rings for high-energy e^+e^- collisions. Richter studied the scaling laws for storage rings in 1976.[2] There are two factors in the cost of a high-energy storage ring. Most of the costs scale as the size of the ring — tunnels, magnets, vacuum systems, etc. The one cost that does not scale with the size of the ring is the rf system, which is required to make up the energy lost to synchrotron radiation. The voltage required to restore the lost energy is proportional to the fourth power of the energy and inversely proportional to the radius of curvature. Thus, simplifying Richter's argument considerably, we can write

$$C = \alpha R + \beta \frac{E^4}{R}, \tag{1}$$

where C is the cost, R is the radius, E is the energy, and α and β are constants. Optimizing the cost by setting the derivative of Eq. (1) with respect to R to zero yields the result that both the cost and size of a storage ring scale with E^2.

We can thus estimate the cost of a 1 TeV storage ring by assuming that LEP II is an optimized 200 GeV storage ring and using this scaling law. The result is that such a ring would be 675 km in circumference and cost 17.5 billion dollars. Even by our new sense of reasonableness set by the SSC scale, this seems unreasonable and suggests that we should pursue an alternate technology. Both the cost and size of a linear collider, of course, scale with energy, making it appear to be a more promising approach.

2.2. Introduction to Linear Collider Parameters

Figure 1 shows a generic linear collider. It has three main accelerators: an electron linac to produce positrons, and positron and electron linacs to accelerate the beams to high energy. It also has two damping rings to reduce

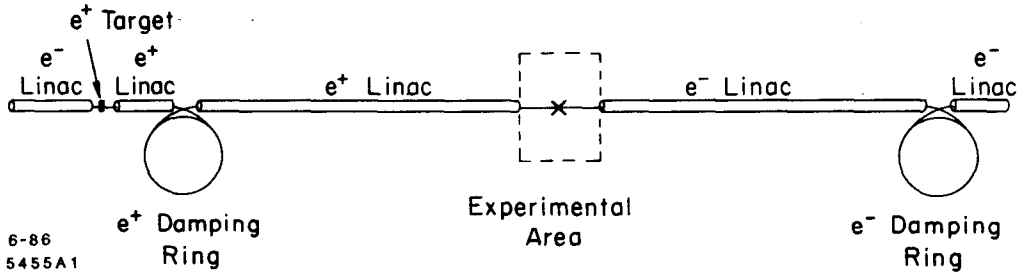

Fig. 1. Schematic of a generic linear collider.

the emittance of the beams, although in some designs the electron damping ring may not be necessary.

Figure 2 shows the only present example of a linear collider, the SLC. Please note that this design is topologically equivalent to the generic linear collider with the present SLAC linac serving as all three required linacs. A positron return line and two arcs have been added to transport the particles to the required locations; in principle, these transport lines do not affect the basic functioning of the collider.

I will not say anything about the SLC in these lectures except to use it as a comparison to the designs for very high-energy colliders. There are two design exercises we can look at: the Cern Linear Collider (CLIC), a 2 TeV collider being designed at CERN,[3] and the TeV Linear Collider (TLC).[4] Table 2 lists some basic parameters of the SLC[5] and these two designs. All three use a conventional travelling wave rf structure for the main accelerator, but differ on the source of rf power. SLC uses conventional klystrons; the CLIC design uses a superconducting drive linac in which a low-energy, high-current electron beam transmits energy to the main linac; and the TLC design envisions using a relativistic klystron in which the low-energy beam is driven by magnetic induction.

The accelerator gradients are considerably higher in the high-energy colliders in order to keep the length reasonable. The TLC design at 196 MV/m is

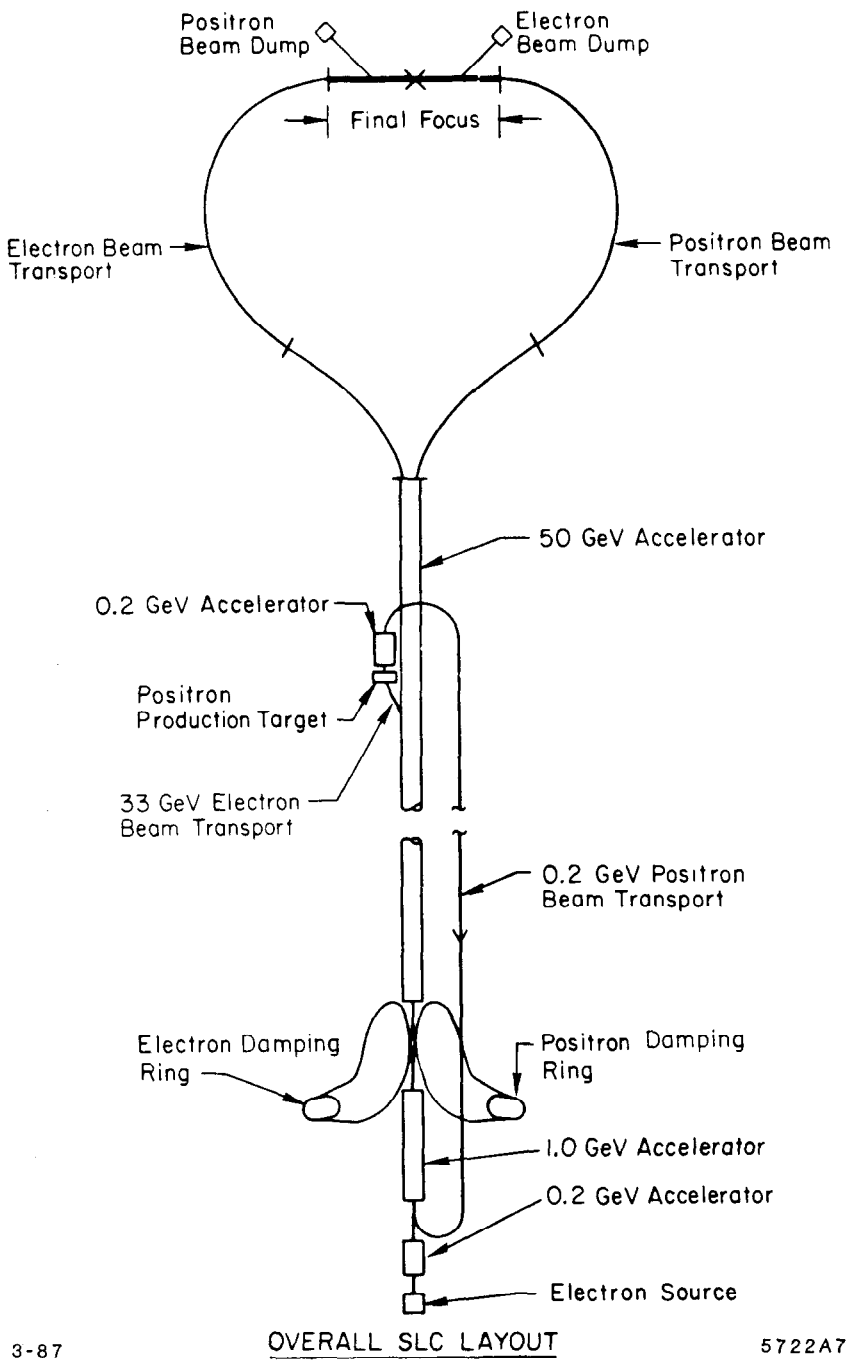

Fig. 2. Schematic of the SLC.

Table 2: Basic Collider Parameters

	SLC	CLIC	TLC
Location	SLAC	CERN (?)	SLAC (?)
Status	Commissioning	Early design studies	
E_{cm}	100 GeV	2 TeV	1 TeV
Power source	Klystron	Superconducting drive linac	Relativistic klystron
Accelerator	Conventional travelling wave rf structure		
Accelerator gradient	17 MV/m	80 MV/m	196 MV/m
Accelerator length	3 km	2×12.5 km	2×2.5 km
Luminosity ($cm^{-2}sec^{-1}$)	6×10^{30}	1.1×10^{33}	1.2×10^{33}

considerably higher than the 80 MV/m envisioned in the CLIC design. Part of the reason for this is to have a design for a 1 TeV collider that would fit on Stanford University land.

The bottom line of Table 2 shows the design luminosities for the SLC and the two designs. The high-energy collider energies are more than two orders of magnitude higher than the SLC luminosity. The reason why this is necessary is most easily seen in Fig. 3, where our present projection of the e^+e^- hadronic cross section is shown. The SLC will run on the peak of Z resonance, while the high-energy colliders will run where the cross section, at least on Fig. 3, is indistinguishable from zero. As we will see later, the 10^{33} $cm^{-2}sec^{-1}$ design luminosities may be insufficient to study the physics of this region. However, these designs are for single bunch operation. By putting more than one electron and positron bunch in the collider on a single rf filling, the luminosity can be increased without using more rf power.

Luminosity is the key parameter of a high-energy collider. It is given by

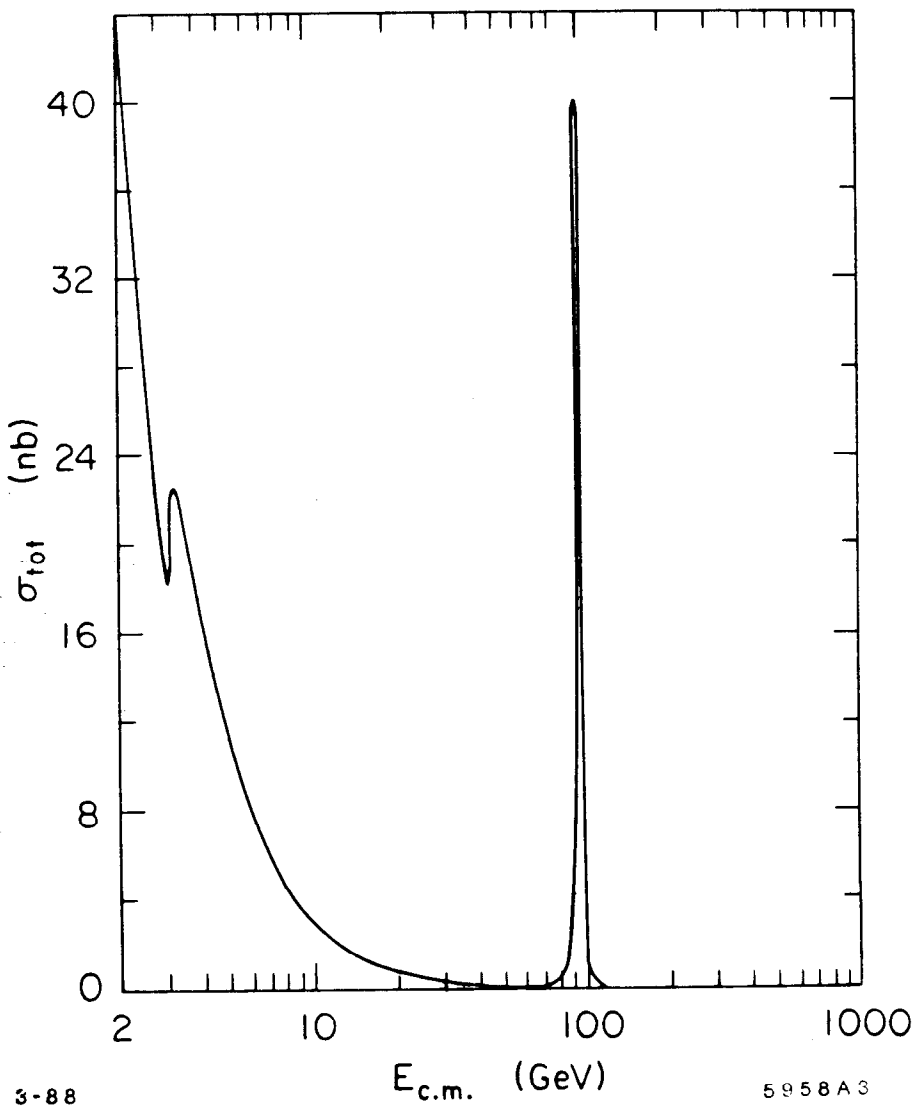

Fig. 3. First-order theoretical cross section for $e^+e^- \rightarrow$ hadrons.

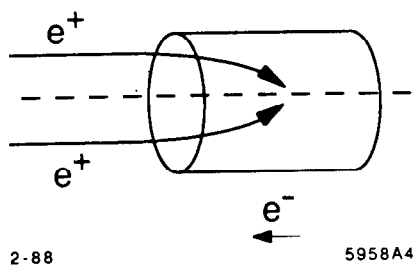

Fig. 4. Focusing of an electron by the charge of the opposite beam.

$$\mathcal{L} = \frac{N_+ N_- f H}{4\pi\sigma_x\sigma_y}, \tag{2}$$

where N_+ and N_- are the numbers of positrons and electrons per bunch, f is interaction frequency, H is an enhancement due to the pinch effect, and σ_x and σ_y are the transverse rms beam sizes at the interaction point. Note that $4\pi\sigma_x\sigma_y$ is just the area of a Gaussian beam.

In the next few subsections, we will examine, one by one, the limitations on the factors that make up the luminosity.[6]

2.3. The Pinch Effect Enhancement H

An off-axis particle in one beam will be focused by the charge of the opposite beam, as illustrated in Fig. 4. This focusing will effectively make the beams smaller at the interaction point, increasing the luminosity.[7] This effect could be incorporated into Eq. (2) by using the effective σ's after focusing, or, as we have done, by using the σ's in the absence of the pinch effect and indicating the effect by the factor H. H is a function of the disruption, D, which is just the ratio of the bunch length to the focal length of the other beam. For round beams, the disruption is given by

$$D = \frac{r_e N \sigma_z}{\gamma\sigma_x\sigma_y}, \tag{3}$$

where r_e is the classical radius of the electron, 2.818×10^{-15} m.

Figure 5 shows a calculation of H as a function of D for both round and flat beams.[8] The pinch effect enhancement for flat beams is approximately the square root of that for round beams, because the pinch occurs only in the thin dimension.

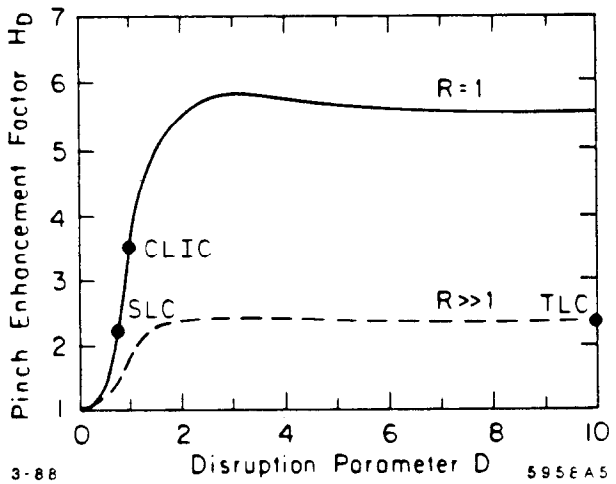

Fig. 5. Pinch enhancement factor H versus disruption D for round (R = 1) and flat (R $\gg$1).

Table 3 shows the disruption and pinch effect enhancement for the SLC and the two high-energy collider designs. The TLC employs flat beams — about which we will comment more shortly — and thus has a lower pinch effect enhancement than CLIC even though it has a much larger disruption. Disruptions larger than 10 may cause plasma instabilities that would blow up the beams and reduce the luminosity.

2.4. The Repetition Rate f

The repetition rate is mainly determined by power, or equivalently, money. For a given design, one can pulse more frequently at the cost of increased power and, possibly, additional components.

Multibunch operation is certainly attractive in principle as a way of increasing the luminosity, but there are technical problems to be solved with wake-field

Table 3: Disruption and Pinch Effect Enhancement

Collider	D	Beam shape	H
SLC	0.76	round	2.2
CLIC	0.91	round	3.5
TLC	10	flat	2.3

control and the requirement that each pulse have the same accelerating field. The latter is required by the necessarily small momentum acceptance of the final focus.

Table 4 gives the repetition rate and beam power in each linac for the SLC and the two high-energy collider designs. The use of a superconducting drive linac in the CLIC design leads to the natural use of a high repetition rate; however, the high repetition rate requires a large number of positrons to be cooled — thirteen 160-m circumference damping rings in the CLIC design. The TLC repetition rate is set by an *ad hoc* limit on wall plug power of 100 MW.

Table 4: Repetition Rate and Beam Power

Collider	f (Hz)	Beam power (MW/linac)
SLC	180	0.10
CLIC	5800	5.0
TLC	90	0.13

2.5. Number of Electrons and Positrons $N_{\pm}$

The number of electrons or positrons per bunch is primarily limited by wake field effects. Transverse wake fields are caused by a beam traveling off center

through the accelerating structure. The tail of the beam sees the fields excited by the head, leading to an apparent emittance growth as shown in Fig. 6.

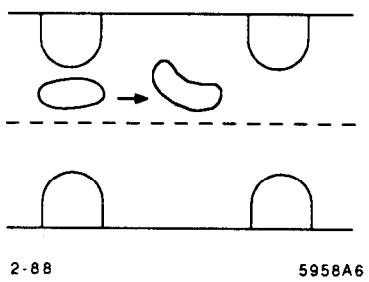

Fig. 6. Wake field effect on a beam traveling off center through an accelerating structure.

For an rf structure that scales as the wave length λ and has focusing that scales as the accelerating gradient E_a, then for the bunch length $\sigma_z \ll \lambda$, the transverse deflection δ_t scales as

$$\delta_t \propto \frac{N\sigma_z}{E_a\lambda^2(\Delta p/p)}. \tag{4}$$

Table 5 shows the bunch length, wave length, and number of particles per bunch for the SLC and the two high-energy collider designs. The accelerating wave length λ has been chosen to be smaller in the high-energy collider designs than at the SLC to allow for increased accelerating gradients and to decrease the stored energy, which scales as λ^2. Because of the long bunch length and short wave length, the CLIC design is much more sensitive to beam misalignment than the TLC design. The criterion used in the TLC design was that the beam position should be controlled to the 30-50 μm level.

2.6. Beam Size $\sigma_{x,y}$

In general, we would like to make σ_x and σ_y as small as possible. The technical challenge is to do so. The beam size at the interaction point is given

Table 5: Bunch Length, Accelerating Wave Length, and Number of Particles per Bunch

Collider	σ_z (μm)	λ (cm)	N (10^9)
SLC	1000	10	70
CLIC	500	1	5.4
TLC	40	2.5	18

by

$$\sigma_{x,y} = \left(\frac{\epsilon_n \beta^\star}{\gamma}\right)^{\frac{1}{2}}_{x,y}, \tag{5}$$

where ϵ_n, is the normalized emittance, *i.e.*, $\epsilon\gamma$, the quantity that is conserved during acceleration, and $\beta^\star$ is the β function, or focal length, at the interaction point.

Table 6 gives the normalized emittance and β functions for the SLC and the high-energy colliders. Both of the high-energy colliders have emittances about an order of magnitude smaller than the SLC, except that the vertical emittance of the TLC is two orders of magnitude smaller still. The vertical emittance of a storage ring is limited mainly by the coupling into the vertical from the horizontal. The technical question is whether this factor of 100 reduction can be both produced and maintained through the acceleration and focusing processes.

Table 6: Emittances and β Functions

Collider	ϵ_{n_x} (m)	ϵ_{n_y} (m)	β_x (mm)	β_y (mm)	σ_x (μm)	σ_y (μm)
SLC	4.2×10^{-5}		5		1.7	
CLIC	2.8×10^{-6}		3		0.065	
TLC	5×10^{-6}	5×10^{-8}	15	0.05	0.27	0.0016

Why is the TLC proposing flat beams rather than the standard round beams? (Note that the standard is set by a single example.) There are a number of reasons:

1. The emittance of damping rings is much smaller in the vertical than in the horizontal.

2. Magnetic quadrupoles focus in one plane while defocusing in the orthogonal plane. Thus an asymmetric focus is natural.

3. A finite crossing angle is needed for high luminosity. This is because in a high-luminosity system the beam disruption will cause the outgoing beam to be larger than the aperture of the final quadrupole. For example, at the TLC the maximum disruption angle is approximately given by

$$\theta_{d_{max}} \approx \frac{2Nr_e}{\gamma\sigma_x} \approx 0.4 \text{ mrad.} \tag{6}$$

This translates into a circle of 220 μm at the face of the first quadrupole, which is located longitudinally 55 cm from the interaction point; however, the inner diameter of these quadrupoles is only 180 μm. A finite crossing angle solves this problem, but creates another one. To avoid losing luminosity,

$$\sigma_x \geq \theta_c \sigma_z, \tag{7}$$

where θ_c is the crossing angle. This condition can be best met by flat beams, as illustrated in Fig. 7. The TLC crossing angle is 6 mrad, which, when combined with the designed beam sizes, meets the above requirement.

2.7. Beamstrahlung

The fourth reason for having flat beams is the effect on beamstrahlung, which we treat here in its own right. In Fig. 4, we showed how particles from one beam see the other beam as a focusing lens. This focusing field produces

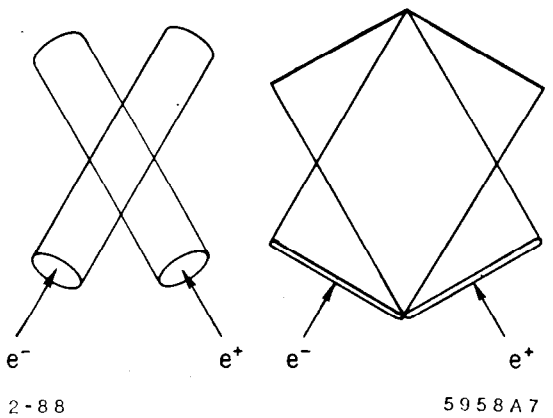

Fig. 7. The effective overlap of different shaped crossing beams.

synchrotron radiation known as "beamstrahlung."[9] The average energy loss by beamstrahlung, δ, is given by[10]

$$\delta = \frac{0.22 r_e^3 N^2 \gamma}{\sigma_z \sigma_y'} \left[\frac{4}{\left(1 + \frac{\sigma_z'}{\sigma_y'}\right)^2} \right] \left(\frac{1}{1 + 1.33 \Upsilon^{\frac{2}{3}}} \right)^2, \tag{8}$$

where

$$\Upsilon = \frac{0.43 r_e^2 N \gamma}{\alpha \sigma_z \sigma_y'} \left(\frac{2}{1 + \frac{\sigma_z'}{\sigma_y'}} \right). \tag{9}$$

The primes on the σ's in the above equations indicate that the pinched values are to be used.

It is clear from the above that flat beams give lower average energy loss. This is because for the areas involved, on the average, the charge is further away. Another way of seeing the same thing is to note that the electric field above and below a flat beam does not change as the thickness of the beam shrinks.

Υ is a measure of the quantum versus classical nature of the beamstrahlung. The last term in Eq. (9) gives the suppression due to quantum effects. This is a factor of eight in the TLC design. Table 7 gives the values of Υ and δ for the three designs.

Table 7: Beamstrahlung Parameters

Collider	Υ	δ
SLC	0.006	0.004
CLIC	0.28	0.19
TLC	1.6	0.27

The solid line in Fig. 8 shows the spectrum of center-of-mass energy after beamstrahlung versus the integrated luminosity for parameters similar to those of the TLC. The average energy loss δ is 0.26. Note that 32% of the spectrum is in the last bin, *i.e.*, there is no beamstrahlung. The dashed line in Fig. 8 shows the effect of multiplying this spectrum by E^{-2} to simulate the effect of the E^{-2} dependence of the cross section for annihilation processes. The resulting rate of production versus energy is approximately flat except for the rise at the maximum energy.

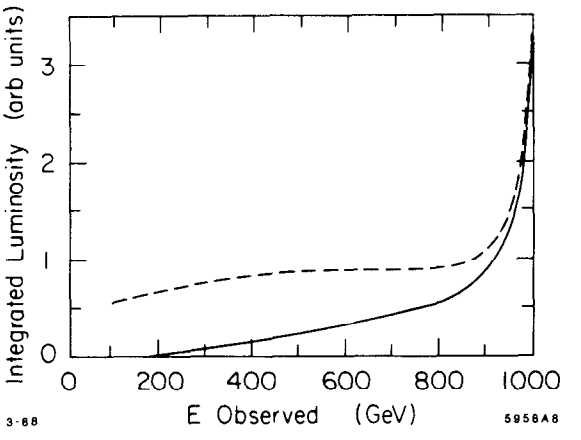

Fig. 8. A typical beamstrahlung spectrum for the TLC design. $\delta = 0.26$. The dashed curve represents the spectrum multiplied by E^{-2} to approximate the cross section for annihilation processes.

An immediate consequence of the spectrum of Fig. 8 is shown in Fig. 9. This figure, prepared by Tom Himel, shows the event rate as a function of

energy if a Z' resonance exists at a mass of 400 GeV/c^2. The couplings of a Z' to e^+e^- are model dependent,[11] but an enhancement of several hundred over the continuum, as shown in Fig. 9, is typical. It is clear from this graph that beamstrahlung makes high-energy linear colliders self-scanning.

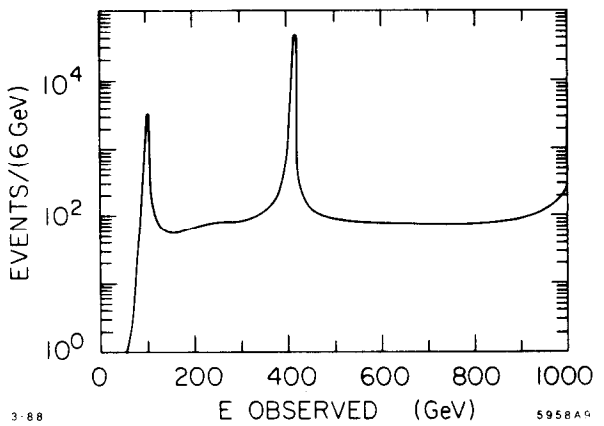

Fig. 9. The event rate for $e^+e^- \rightarrow$ hadrons in the TLC if a Z' resonance with mass of 400 GeV/c^2 exists.

I will not discuss Z' resonances further in these lectures, because they are clearly very easy to find, and the physical measurements that one would make are quite similar to those that will be made on the Z by the SLC and LEP. If we were to discover a Z' resonance at the Tevatron or the SSC, then we could consider building a dedicated e^+e^- linear collider to study it. This collider could have lower luminosity than the luminosities we are considering here and would, consequently, be much simpler to build and operate.

2.8. Longitudinal Polarization

Since many processes are strongly polarization dependent,[1] it will be extremely useful to have longitudinally polarized electron beams. This can be done in a similar manner to the way it is being accomplished in the SLC.[12] However, we must consider whether the beam-beam disruption will destroy the

polarization. The precession angle is related to the disruption angle by

$$\Delta\theta_{pol} = \frac{g-2}{2}\gamma\theta_{dis}. \tag{10}$$

The maximum disruption angle is given by

$$\theta_{d_{max}} = k\frac{Nr_e}{\gamma\sigma_x} \quad \begin{cases} k \approx 1 & \text{for round beams} \\ k \approx 2 & \text{for flat beams.} \end{cases} \tag{11}$$

The cosine of the precession angle is approximately the depolarization factor. Table 8 gives the maximum disruption angles, and the maximum precession angles and their cosines. It is clear that the depolarization effects are small in all cases.

Table 8: Maximum Disruption and Polarization Precession Angles

Collider	$\theta_{d_{max}}$	$\Delta\theta_{pol}$	$\cos\Delta\theta_{pol}$
SLC	1.2×10^{-3}	0.13	0.99
CLIC	1.2×10^{-4}	0.27	0.96
TLC	3.8×10^{-4}	0.44	0.91

2.9. Summary of Parameters

Table 9 brings together all of the parameters we have discussed into a single table for reference.

2.10. Experimental Consequences

There are two main experimental consequences of the TLC design that we have had to incorporate into our simulations of TLC physics. First, we have used beamstrahlung spectra with $0.22 < \delta < 0.26$. We have used two approaches to deal with beamstrahlung. In most analyses, we have given up

Table 9: Summary of Collider Parameters

	SLC	CLIC	TLC
Location	SLAC	CERN (?)	SLAC (?)
Status	Commissioning	Early design studies	
$E_{c.m.}$ (TeV)	0.1	2	1
Power source	Klystron	Superconduct. drive linac	Relativistic klystron
Accelerator type	Conventional travelling wave rf structure		
Accelerator gradient (MV/m)	17	80	196
Accelerator length (km)	3	2×12.5	2×2.5
Rf wavelength (cm)	10	1	2.5
Repetition rate (Hz)	180	5800	90
Particles per bunch	7×10^{10}	5.4×10^{9}	1.8×10^{10}
Beam power (MW)	2×0.10	2×5	2×0.13
Horiz. emittance ϵ_x (rad m)	4.2×10^{-5}	2.8×10^{-6}	5×10^{-6}
Vert. emittance ϵ_y (rad m)	4.2×10^{-5}	2.8×10^{-6}	5×10^{-8}
$\beta_x{}^\star$ (mm)	5	3	15
$\beta_y{}^\star$ (mm)	5	3	0.05
Bunch width $\sigma_x{}^\star$ (μm)	1.7	0.065	0.270
Bunch height $\sigma_y{}^\star$ (μm)	1.7	0.065	0.0016
Bunch length σ_z (mm)	1	0.5	0.04
Disruption	0.76	0.91	10
Pinch enhancement	2.2	3.5	2.3
Quantum radiation param. Υ	6×10^{-3}	0.28	1.6
Beamstrahlung δ	4×10^{-3}	0.19	0.27
Max. disruption angle (mrad)	1.2	0.12	0.38
Max. polariz. rotation (rad)	0.13	0.27	0.44
Luminosity ($cm^{-2}sec^{-1}$)	6×10^{30}	1.1×10^{33}	1.2×10^{33}

on the constraints on $E_{c.m.}$ and $(p_z)_{c.m.}$ and have just used the conservation of transverse momenta, as is done in hadron colliders. In one analysis I will discuss (charged Higgs bosons), all of the constraints were retained in a mild way by only using events in which the visible energy was approximately equal to the total energy.

The second consequence has to do with the forward direction. Since the final quadrupoles in the TLC design are only 55 cm from the interaction point, since these quadrupoles have to be supported on actively vibration-damped supports, and since the design has crossing beams, we have assumed that no particles are detected within 10° of the incident beams. It is probable that we will be able to do some particle detection in this region, but we wanted to be conservative and see whether this condition prevented us from doing any physics.

3. Detector Requirements

3.1. Calorimetry

Much of the physics of the TLC will require the detection of W's and Z's. These particles will be the "pions" of lower-energy colliders. We will want to be able to detect them in their hadronic decays for two reasons:

1. The rate is higher. Seventy-five per cent of W decays and 85% of visible Z decays go into hadrons.
2. The W leptonic decay, $W \rightarrow \ell\nu$, has undetected neutrino energy. Thus, we lose a usually required constraint and we cannot reconstruct masses.

The key to reconstructing W and Z masses is a well-segmented hadronic calorimeter. To study how much segmentation is needed, I have made a crude study. An n° by n° cell was simulated by first combining all hadrons within 0.75n° into a single combination and then randomly moving the combination in an angular box n° by n° centered on the direction of the momentum vector of the combination. This should be a reasonable estimate of a n° by n° cell

calorimeter. The energy resolution of the calorimeter is taken to be $0.5/\sqrt{E}$. We will return to the question of energy resolution shortly.

We will use W mass reconstruction as a criterion. The analysis proceeds as follows:

1. Lorentz transform the event along the direction of the incident beams (z-axis) so that $\sum \vec{p}_z = 0$, where the sum is over the visible charged and neutral particles. This simply removes the effect of beamstrahlung as much as possible to facilitate the next step.
2. Divide the event into two hemispheres using the thrust axis.
3. Require that $|\cos\theta_{thrust}| < 0.8$. This requirement eliminates events in which a substantial number of particles may be lost in the 10° hole around the beam pipe.
4. Calculate the invariant mass in each hemisphere.

Figure 10 shows a scatter plot of the resulting mass in each hemisphere for $e^+e^- \rightarrow WW$ events (for 4° cells). Figure 11 shows a projection of Fig. 10 on one axis when the mass projected on the other axis is within 10 GeV/c^2 of the W mass. Two criteria of quality are the full width at half maximum (FWHM) of the distribution and the number of events retained within 10 GeV/c^2 of the W mass in both hemispheres. These quantities are plotted in Fig. 12 versus the cell size.

Figure 12 shows that 4°×4° cells work well. This is clearly a practical size, as it is the approximate segmentation of the SLD calorimeter.[13]

The above results were obtained using an energy resolution of $0.5/\sqrt{E}$. This is an adequate resolution, but an important point about calorimeters at high energy should be noted. In general, one can approximate the energy of a calorimeter by

$$\frac{\delta E}{E} = \frac{a}{\sqrt{E}} + b. \tag{12}$$

If $a = 0.50$, then at an energy of 1 TeV, b must be less than 0.015 so as not to dominate the $a/\sqrt{E}$ term. Wigmans has shown than an e/π response

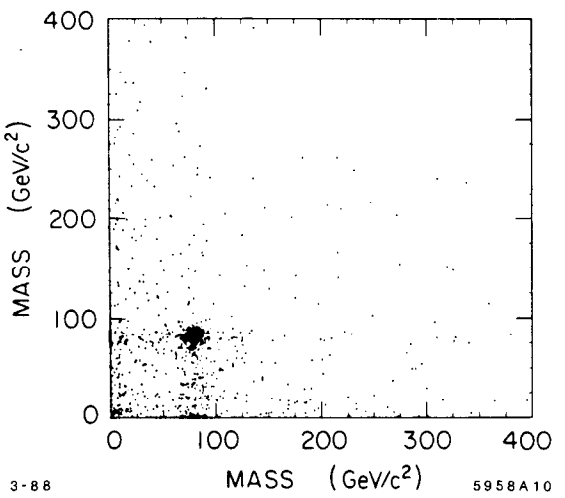

Fig. 10. The invariant mass in each hemisphere for $e^+e^- \rightarrow WW$ events as measured by a calorimeter with 4° cells.

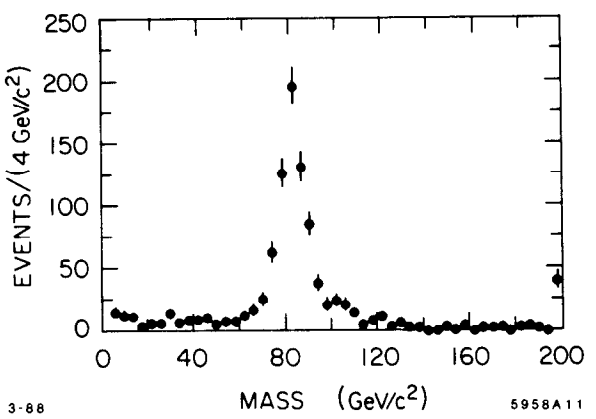

Fig. 11. The projection on one axis of Fig. 10 when the projection on the other axis is within 10 GeV/c^2 of the W mass.

that differs from unity will set a lower limit on b.[14] For example, the lead-liquid argon SLD calorimeters have an e/π response of 1.24, which implies that $b \geq 0.045$. To get $b < 0.015$, the e/π response must lie between 0.9 and 1.1. It is now known how to build a variety of calorimeters that meet this condition.[14]

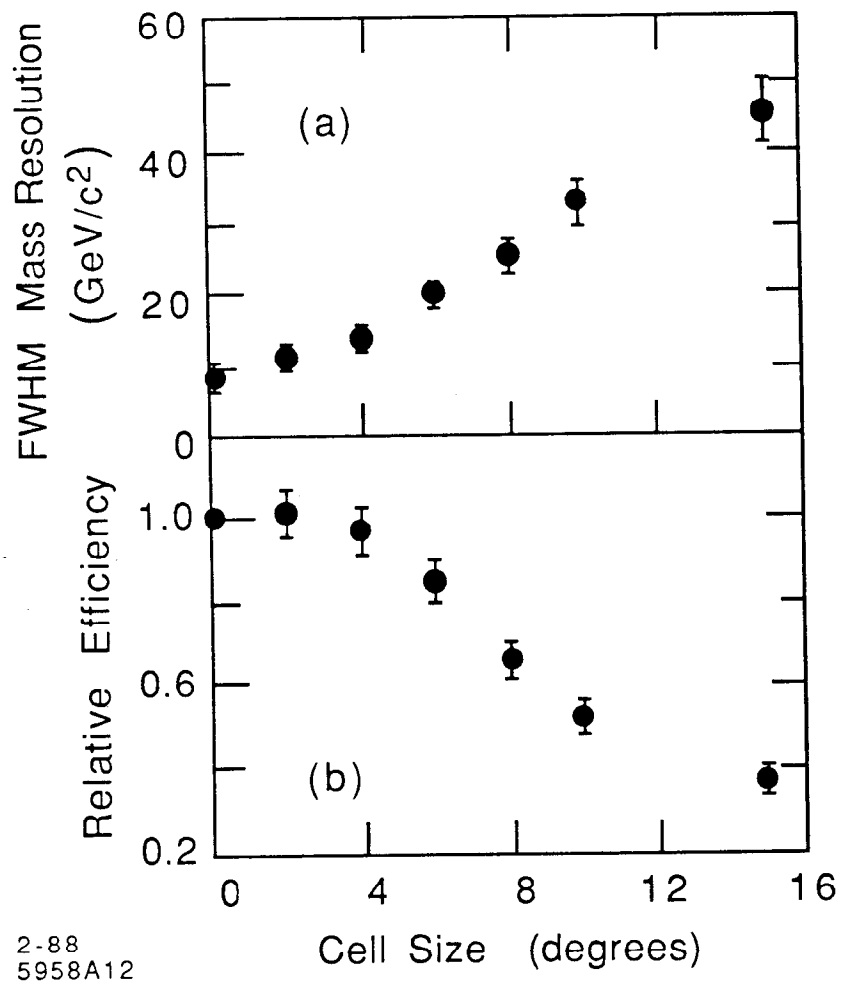

Fig. 12(a). The FWHM resolution of a reconstructed W versus the cell size. (b) The relative efficiency for both W's to be reconstructed within 10 GeV/c^2 of the W mass.

3.2. Charged Particle Tracking

Another requirement we will have is to measure 500 GeV leptons relatively well. A charged particle momentum resolution of $\Delta p/p = 3 \times 10^{-4}$, ($p$ in GeV/c) yields an rms resolution of 15% at 500 GeV/c, which is quite adequate. Scaling from the Mark II design and using a tight vertex constraint, one can achieve this with a drift chamber with the following parameters:

1. a radius of 1.8 m,
2. a B field of 1.0 T, and
3. 72 layers with 200 μm resolution on each layer.

These parameters are relatively easy to achieve.

Shortly we will see another reason for very good pattern recognition.

4. General Physics Environment

4.1. The Basic Processes

To understand the general physics environment we will face at the TLC, we will look at the two major annihilation processes:

$$e^+e^- \rightarrow q\bar{q} \tag{13}$$

and

$$e^+e^- \rightarrow W^+W^-. \tag{14}$$

Pat Burchat has prepared some plots of these processes at a center-of-mass energy of 1 TeV with detector smearing, beamstrahlung, and bremsstrahlung for 2 fm^{-1} of data (Figs. 13-16). For orientation, this amount of data would be accumulated in 2 months of running at an average luminosity of 4×10^{32} $cm^{-2}sec^{-1}$.

Table 10 gives the first-order cross sections and the actual observed cross sections for these processes and the smaller Z pair production process. As usual, the cross sections are given in terms of R, the ratio between the cross section and the first-order electromagnetic μ-pair production cross section. There is a large difference between the first-order cross section (R_0) and the observed cross section (R). This is partially due to the effect of beamstrahlung, which effectively reduces the center-of-mass energy and thus increases the cross section. In the case of quark-pair production, the bulk of the observed cross section is due simply to the production of the Z and a hard photon. We will see that it is easy to discriminate this relatively uninteresting process.

Table 10: First-order and Actual Cross Sections for the Major Annihilation Processes

Process	R_0	R	Events/2 fb^{-1}
$e^+e^- \rightarrow q\bar{q}$	8.9	46.2	8000
$e^+e^- \rightarrow W^+W^-$	26.6	41.1	7100
$e^+e^- \rightarrow ZZ$	1.5	2.4	400

Figures 13, 14, and 16 show quantities for reactions (13) and (14), the former on the top half of the figure and the latter on the bottom half. Figure 13 shows the visible energy, the invariant mass of the visible particles, and the cosine of the trust axis. The quark-pair (*i.e.*, hadron) production is dominated by the before-mentioned process of radiating to the Z. This process gives a strong forward peaking and invariant masses of at most the Z mass. The W pair production is also strongly forward peaked because it is dominated by the diagram in which a neutrino is exchanged. Most of the new physics that we will be searching for will occur in the central region. To see this region more clearly, in Figures 14 through 16 we apply two cuts, as indicated on Figure 13:

$$\cos\theta_{thrust} \leq 0.8, \tag{15}$$

and

$$m \geq 0.3 E_{c.m.}, \tag{16}$$

where m is the invariant mass of all of the visible particles.

Figures 14(a) and (b) show the charged multiplicity. For quark-pair production, the average charged multiplicity is 41, about twice as large as it is on the Z. For W-pair production, the average charged multiplicity is 29, but this is made up of three distinct cases: Six per cent of the events have both W's decay leptonicly and have low multiplicity, typically 2; about 40% of the events have one W decay leptonicly and the other hadronicly, giving a charged multiplicity of slightly more than 20; and the remainder of the events have both W's decay hadronicly, yielding a charged multiplicity of about 40, similar to the quark-pair case.

Figures 14(c) and (d) show the invariant mass of each hemisphere defined by the plane normal to the thrust axis. The bump at the Z mass in quark-pair production is due to the fundamental process $e^+e^- \rightarrow Z\gamma$ at large angles, so that it satisfies conditions (15) and (16). This process can be easily separated from normal quark-pair production, as will be seen in Figure 15. The quark-pair production jet masses peak around 40 GeV/c^2 with a long tail due to gluon production. In contrast, the invariant masses in each hemisphere from W-pair production peak sharply at the W mass with small tails due to confusion from backward-going particles.

Figure 15 shows scatter plots of the masses in each hemisphere for each of the three processes listed in Table 10. It is clear that W-pair events can be separated from quark-pair production rather cleanly by this technique alone. The Z-pair production appears to be lost in the tails of the more copious processes, but we will see shortly that there is even a possibility of separating it in its hadronic decay modes.

Figure 16 shows various measures of transverse momentum. In Figs. 16(a) and (b) the sum of the transverse momentum of visible particles is plotted. There is a substantial tail beyond 40 GeV/c from neutrino production. Figures

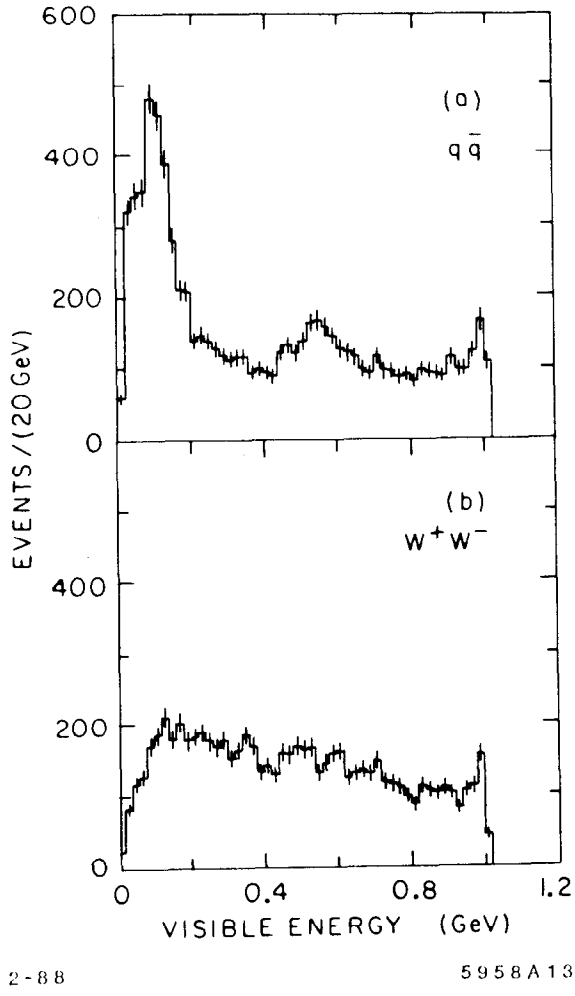

Fig. 13(a-b). The visible energy for (a) quark-pair production and (b) W-pair production.

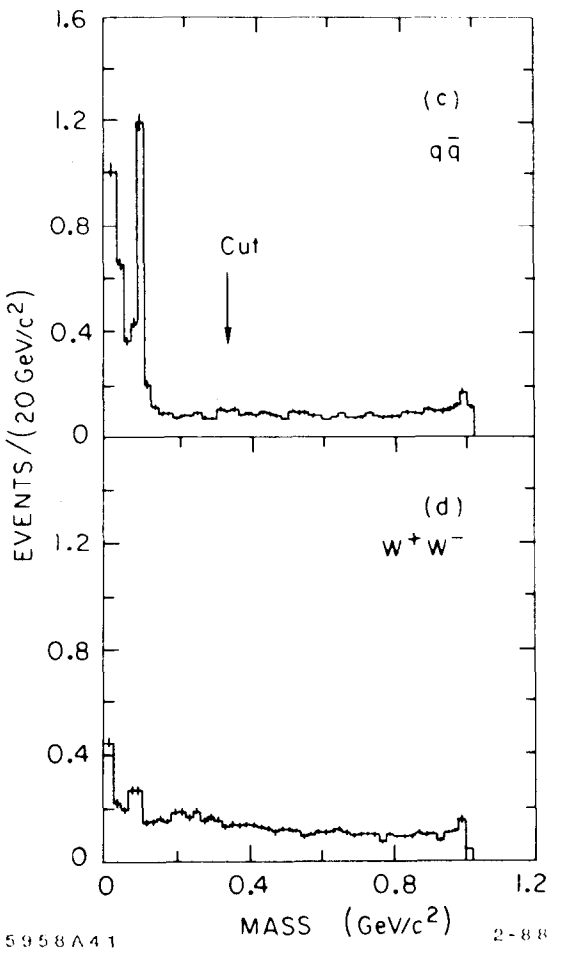

Fig. 13(c-d). The visible invariant mass for (c) quark-pair production and (d) W-pair production.

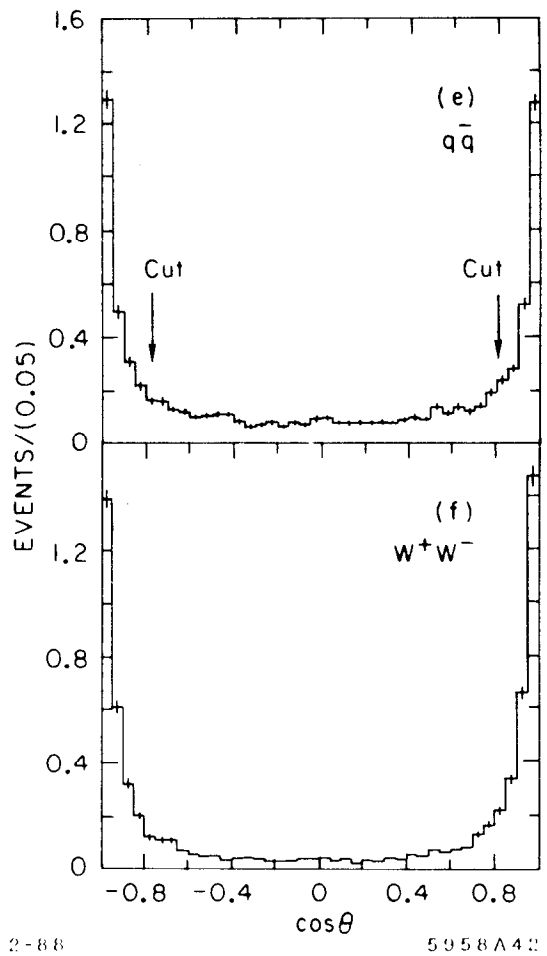

Fig. 13(e-f). The cosine of the thrust axis for (e) quark-pair production and (f) W-pair production.

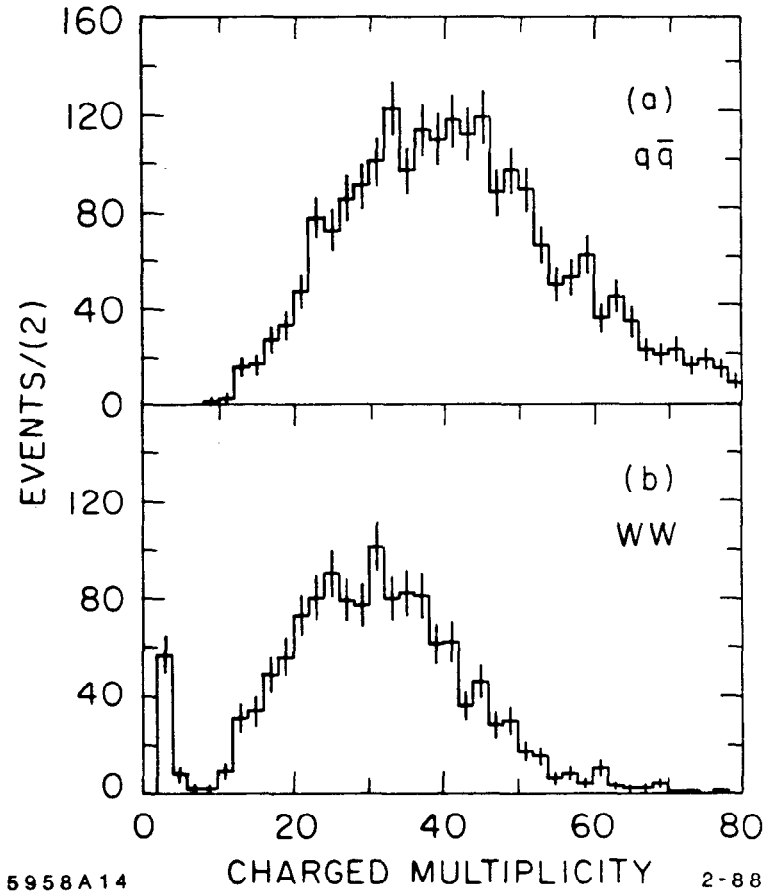

Fig. 14(a-b). The charged multiplicity for (a) quark-pair production and (b) W-pair production.

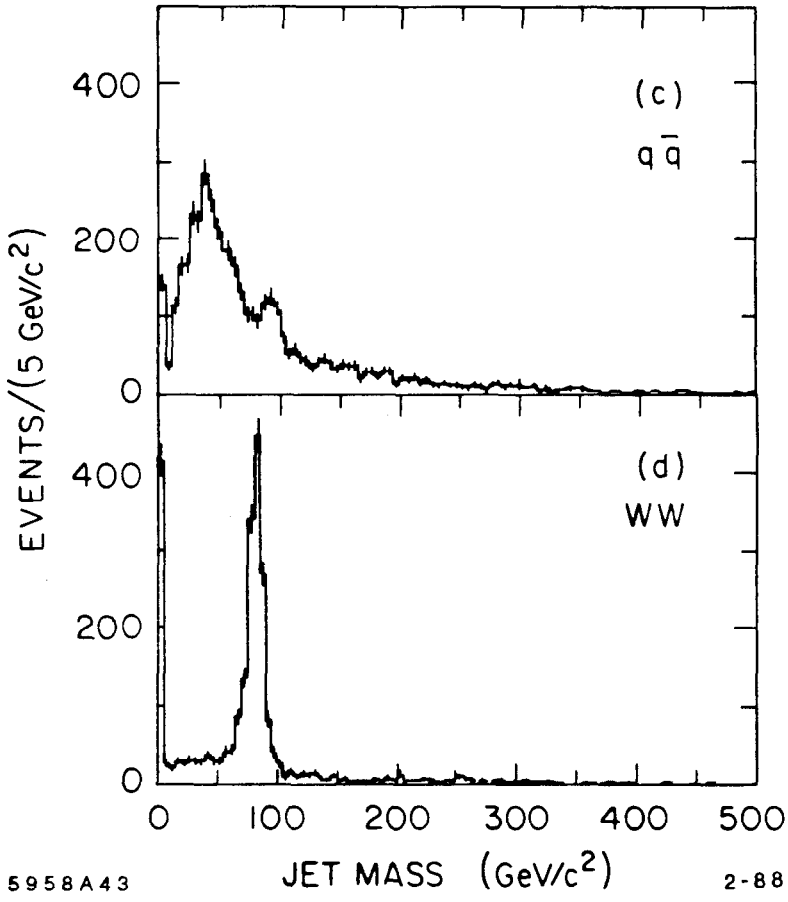

Fig. 14(c-d). The jet mass in each hemisphere defined by the normal to the thrust axis for (c) quark-pair production and (d) W-pair production.

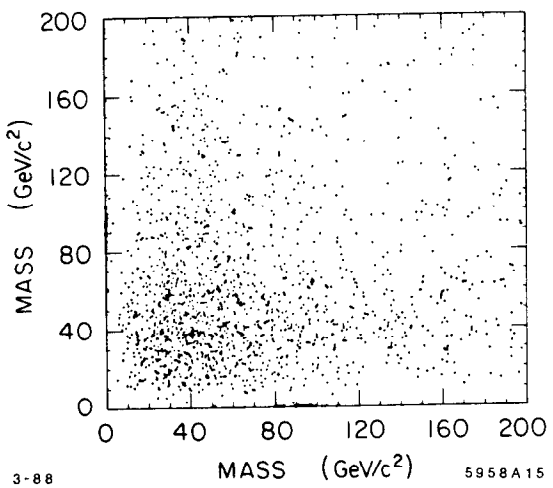

Fig. 15(a). Scatter plot of the jet mass in each hemisphere defined by the normal to the thrust axis for quark-pair production.

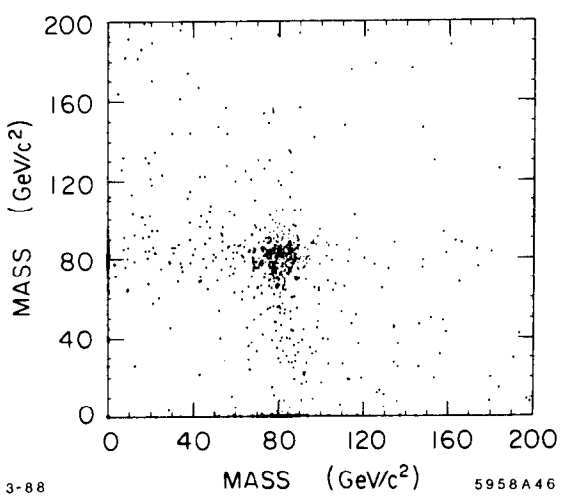

Fig. 15(b). Scatter plot of the jet mass in each hemisphere defined by the normal to the thrust axis for W-pair production.

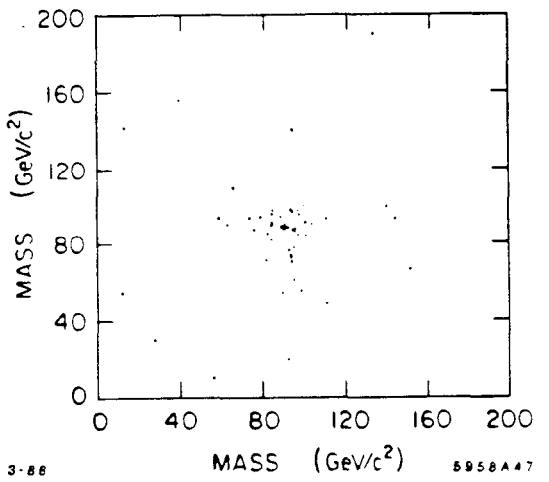

Fig. 15(c). Scatter plot of the jet mass in each hemisphere defined by the normal to the thrust axis for Z-pair production.

16(c) and (d) differ in plotting the momentum transverse to both the incident beams and the thrust axis. Here there is no tail beyond 40 GeV/c, because neutrinos are emitted preferentially in the thrust direction. A somewhat equivalent variable is plotted in Figs. 16(e) and (f), the acoplanarity angle of the sum of the momentum in each hemisphere. There are relatively few events beyond 10° for quark-pair production and 20° for W-pair production. The moral of Fig. 16 is that when searching for new processes for which non-zero transverse momentum is a signature, it is generally better to use either the transverse momentum normal to the thrust axis or the acoplanarity angle as a discriminant rather than just the transverse momentum.

4.2. Note on the Top Mass

In almost all of our simulations we have used the now unfashionable value of 40 GeV/c^2 for the top quark mass. A more fashionable (and interesting) value is $m_t \approx m_W$. In this case the top quark would decay to three jets, but one of the jets would likely be soft and the decay would look very much like a W decay. However, the semileptonic top quark decay would still look different from W decay because the lepton from top decay would not be isolated.

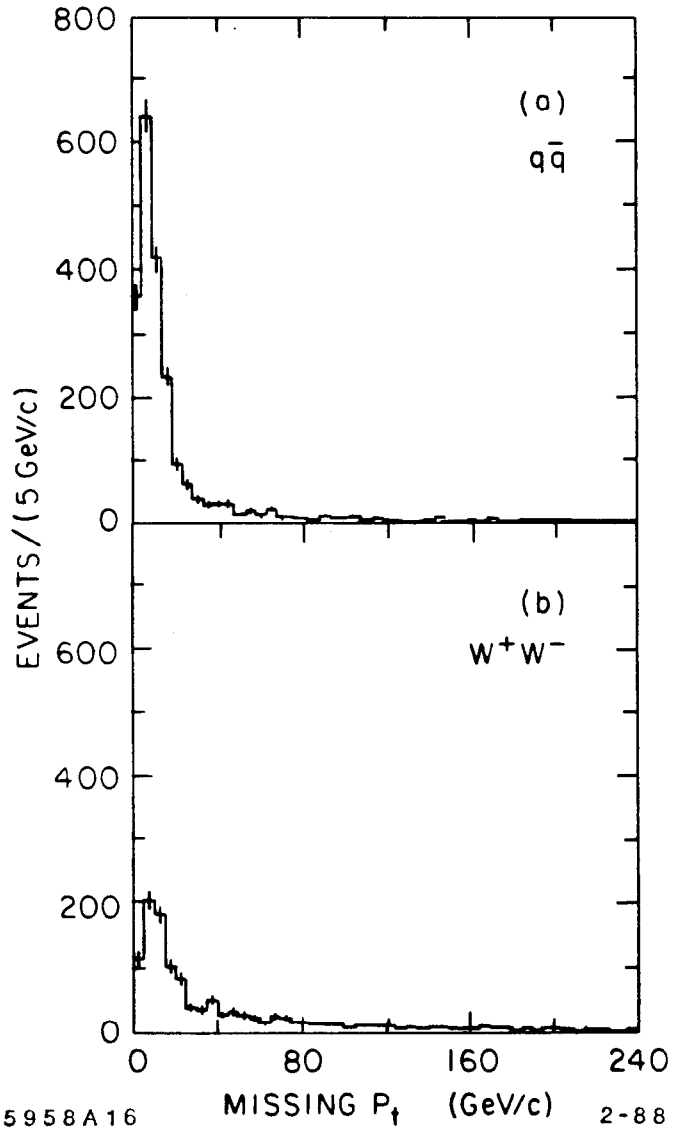

Fig. 16(a-b). The event transverse momentum for (a) quark-pair production and (b) W-pair production.

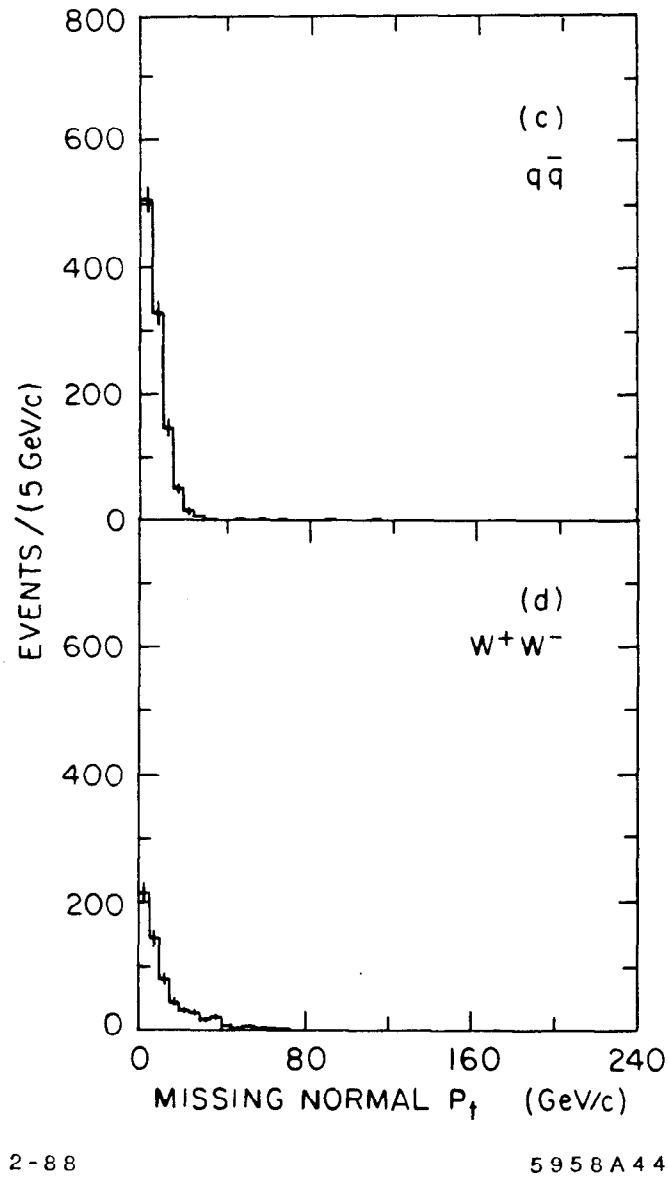

Fig. 16(c-d). The event transverse momentum normal to both the incident beams and the thrust axis for (c) quark-pair production and (d) W-pair production.

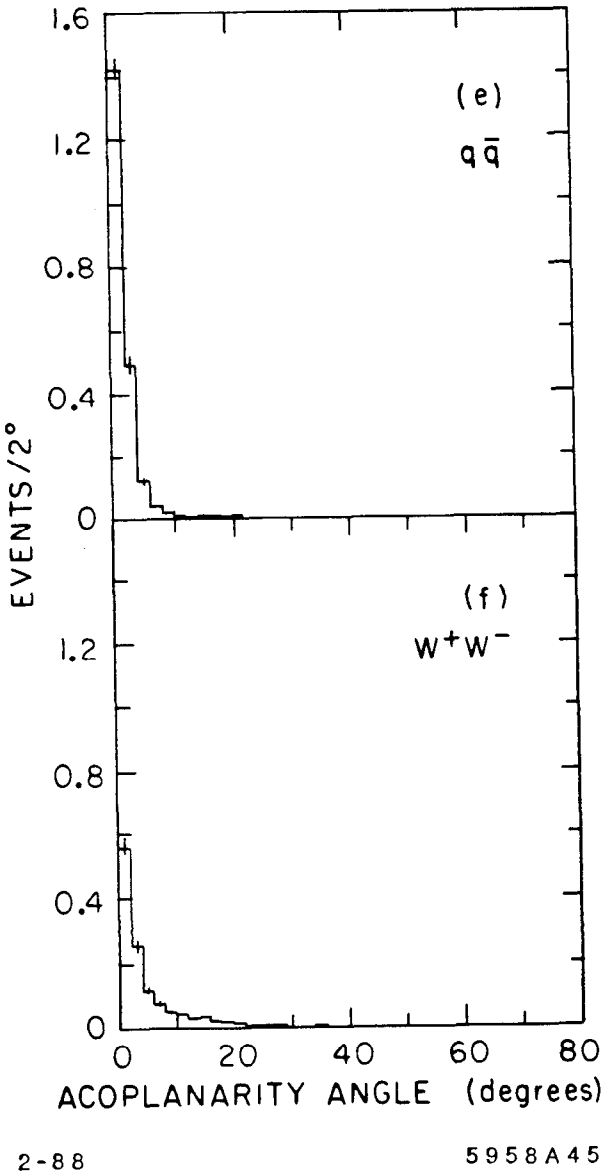

Fig. 16(e-f). The acoplanarity angle for (e) quark-pair production and (f) W-pair production.

4.3. Two-Photon Processes

Figure 17 shows diagrams for two-photon or "$\gamma\gamma$-fusion" production of quark and W pairs. The cross section for hadron production is enormous, but the mass of the system is small. This will not be any more of a problem at the TLC than it has ever been in e^+e^- annihilations.

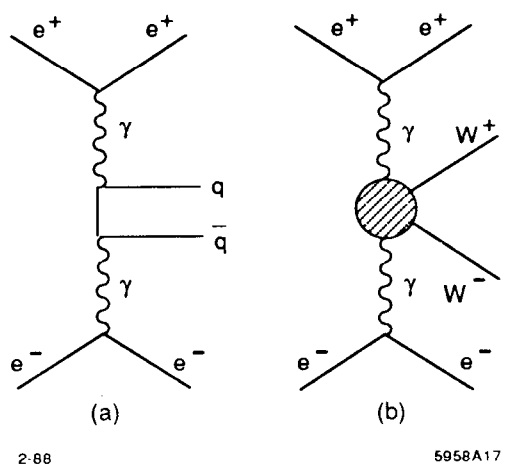

Fig. 17. Diagrams for (a) $q\bar{q}$ and (b) W^+W^- production by $\gamma\gamma$ fusion. The scattered e^+ and e^- in general go forward and are not detected. The shaded area in (b) represents the sum of all gauge-invariant couplings.

The production of W pairs by $\gamma\gamma$ fusion received a great deal of attention at the La Thuile Workshop,[15] but it will be unimportant for our purposes because the electrons have no transverse momenta and go forward. Thus this process looks exactly like $e^+e^- \rightarrow W^+W^-$ in the presence of beamstrahlung, except that it is softer and has a smaller cross section. Figure 18 shows the invariant mass spectrum of W pairs from $\gamma\gamma$ fusion. It is to be compared with Figure 13(e). Note that the W^+W^- invariant mass spectrum is much flatter, varying from 200 to 100 events per 20 GeV/c^2 bin from threshold to 1 TeV/c^2. Table 11 gives a comparison of the cross sections.

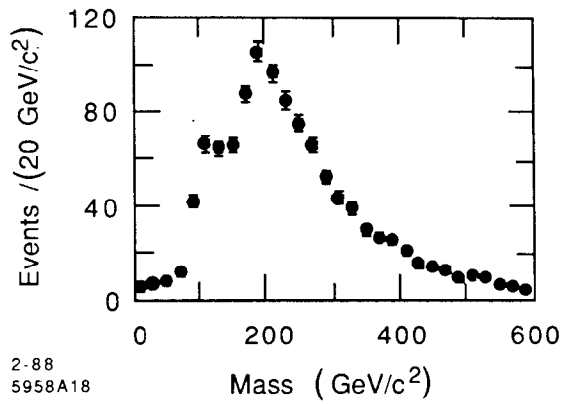

Fig. 18. The invariant mass spectrum of W pairs from $\gamma\gamma$-fusion production of W pairs. The figure represents 2 fb^{-1} of data at 1 TeV center-of-mass energy.

Table 11: Cross Sections for W^+W^- Production from the Annihilation and the $\gamma\gamma$ Processes Including the Effects of Beamstrahlung

Process	R	R ($m_{vis} > 0.3$)
$e^+e^- \rightarrow W^+W^-$	41	28
$e^+e^- \rightarrow W^+W^-e^+e^-$	7	1.8

Based on these results, we can safely ignore the $\gamma\gamma$-fusion production of W pairs. However, we will shortly see that this will not be the only source of fusion background.

5. W Pair Production

5.1. Introduction

Mike Peskin has shown us that the gauge cancellations in W-pair production make it sensitive to new physics.[1] We thus want to be able to measure the angular distribution as accurately as possible.

There are two ways of approaching this analysis — by either looking at the case in which both W's decay into hadrons or the case in which one hadron decays to hadrons and the other decays leptonicly. These two techniques give approximately the same number of analyzed events, as shown in Table 12.

Table 12: Branching Fractions and Efficiencies for Two Methods of Studying W^+W^- Production

	Both W's decay into hadrons	One W decays into hadrons and the other decays into leptons
Branching Fraction (B)	$B_h = 0.56$	$2(B_{e\nu} + B_{\mu\nu})B_h = 0.25$
Efficiency (ϵ)	0.20	0.53
$B \cdot \epsilon$	0.11	0.13

5.2. All Hadronic Decays

Detection via the hadronic decays of both W's have the following advantages and disadvantages relative to the alternative.

1. The hadronic method has no kinematic ambiguity and allows a two constraint fit. We will see shortly that using one leptonic decay introduces a quadratic ambiguity in the reconstruction.
2. The hadronic method is relatively free of background, but not as completely background-free as the alternative.
3. The conventional wisdom is that the charge of the W's cannot be measured using the all hadronic decays.

It is worth examining whether this last statement is really true. It must be remembered that W's are not like quarks — they have no soft gluon radiation. Kinematically, a W at the TLC is almost like a τ at PEP. No one has every had any difficulty determining the sign of a τ at PEP, so we may reasonably ask

the question of whether it is possible to determine the sign of a W that decays into hadrons at the TLC.

There are two related questions that we have to ask:

1. Can we determine the charge with high reliability if we have perfect tracking?
2. And, if the answer to above question is yes, how good does our tracking have to be and can we achieve it?

The answer to the first question is given by Fig. 19 and Table 13. The analysis outlined in Section 3.1 is performed (divide each event into two hemispheres with the thrust axis and calculate the invariant mass in each hemisphere) giving a the result shown in Fig. 10. Then W-pair events are selected by requiring that each hemisphere has an invariant mass within 10 GeV/c^2 of the W mass. The total charge measured for the whole event is required to be zero and the absolute charge in each hemisphere is plotted in Fig. 19. Note that the only time we make a mistake is when two particles cross into the wrong hemisphere since we can discard the $|Q| = 0$ and $|Q| = 2$ events. The fraction of mistakes is monitored then by the number of events in the $|Q| = 3$ bin, less than 1%. These results are summarized in Table 13.

Table 13: Number of Signal and Background Events for W^+W^- Analysis with and without a Charge Measurement for 3.5 fb^{-1} of Data

	No charge measurement		Charge measurement	
Process	# of events all charges	% Background	# of events $\|Q\| = 1$	% Background
$e^+e^- \rightarrow W^+W^-$	499		417	
$e^+e^- \rightarrow q\bar{q}$	32	6.5%	10	2.4%
$e^+e^- \rightarrow ZZ$	17	3.4%	3	0.8%
Total background	49	9.9%	13	3.2%

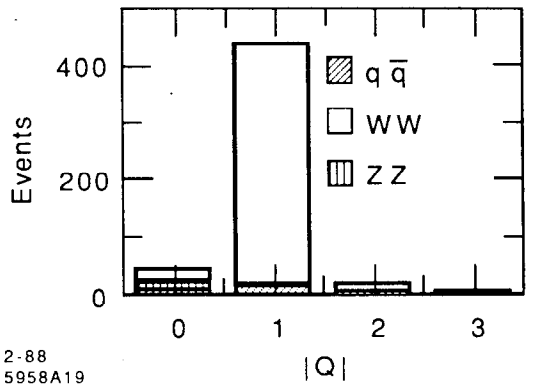

Fig. 19. The charge in each hemisphere when the invariant mass in each hemisphere is within 10 GeV/c^2 of the W mass and the total charge measured in the event is zero.

For amusement sake, Fig. 20 shows what happens if one applies the same analysis to Z pairs. The mass cut is now made about the Z mass instead of the W mass. There is considerable background, but the Z pairs do dominate the $|Q| = 0$ bin.

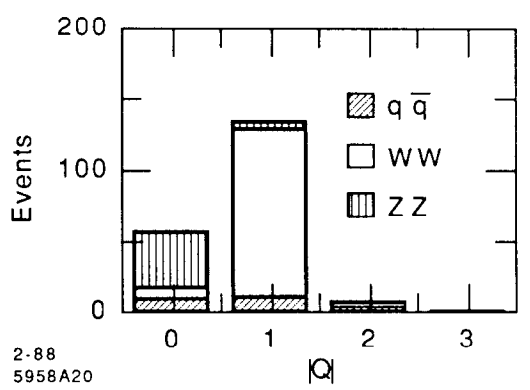

Fig. 20. The charge in each hemisphere when the invariant mass in each hemisphere is within 10 GeV/c^2 of the Z mass and the total charge measured in the event is zero.

Having answered the first question affirmatively, we can turn to the second question. To track 40 particles correctly 90% of the time, we need 99.7% tracking efficiency on a single track. Is this possible? One of the limitations of tracking is that particles decay and the resulting kink can confuse the tracking some of the time. The average probability of π or K decay is about 0.25% and 2% per particle, respectively. I do not know that tracking to this level is not possible, but it certainly represents a challenge to drift chamber design and tracking. We will see other applications of this type of tracking ability as we proceed.

5.3. One Hadronic Decay and One Leptonic Decay

Rick Van Kooten has analyzed this case. We have three missing pieces of information — the three components of the neutrino momentum — and we have three constraints:

$$\sum p_x = 0 \tag{17}$$

$$\sum p_y = 0 \tag{18}$$

$$m_{\ell\nu} = m_{\mathrm{W}}. \tag{19}$$

Thus, this is a 0-C fit, but with a quadratic ambiguity since we have no way of knowing the sign of the missing longitudinal neutrino momentum. Does this ambiguity affect our resolution?

The analysis proceeds as follows:

1. Require an isolated lepton by requiring that there be less than 2 GeV of additional energy within a 30° cone of the lepton.

2. Do a cluster analysis with a minimum separation of 15 GeV between clusters. Require that each cluster have $|\cos\theta| < 0.8$ and require that there be two clusters with a combined invariant mass within 10 GeV/c^2 of the W mass.

3. Reconstruct p_ν up to the quadratic ambiguity. Reject imaginary values of p_ν and resolve the ambiguity by choosing the smaller value of $|p_\nu|$.

4. Boost the event along the z axis so that $\sum \vec{p}_z = 0$, where the sum includes p_ν.

5. Using the lepton sign, plot the angular distribution.

This analysis is almost completely clean. The background from quark-pair production is less than 0.1% (no events in a 10,000 event Monte Carlo simulation) and about 0.1% from Z-pair production. Figure 21 shows the results compared to the input values and to values that would occur if the W had an anomalous magnetic moment.[1]

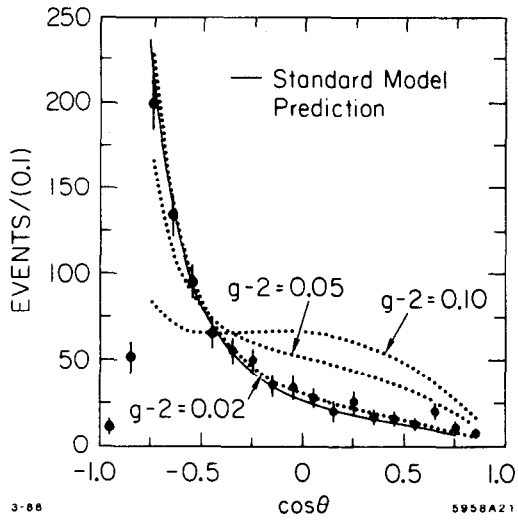

Fig. 21. The reconstructed angular distribution of W pairs from the case in which one W decays hadronicly and the other W decays leptonicly. The solid line shows the input distribution and the dotted lines indicate possible results if the W were to have an anomalous magnetic moment.

6. Heavy Quarks

6.1. Introduction

We will start exploring the discovery potential of the TLC by looking at the detection of heavy quarks. This is a rather easy problem for the TLC and will serve as a warm-up exercise.

In this and the other topics to follow, all of the results will be quoted for 30 fm^{-1} of integrated luminosity. This corresponds to 3×10^{33} $cm^{-2}sec^{-1}$for a nominal year of 10^7 seconds.

We make no claim of having optimized the analyses in the topics that follow. More sophisticated analyses are certainly possible. In some cases, our exercise was to see how unsophisticated one could be and still see signals.

A previous study of heavy quark production in the TLC was done by Jonathan Dorfan and Rick Van Kooten.[16] The analysis presented here differs somewhat by incorporating the experimental conditions that we specified in Section 2.10 and by being a little simpler and thus more suited to a pedagogical discussion.

We assume the existence of a b′ quark of mass 150 GeV/c^2 and, optionally, a t′ quark of mass 200 GeV/c^2. The cross sections and decay modes of these heavy quarks are given in Table 14.

Table 14: Cross sections and Decay Modes of Heavy Quarks

Type	Mass (GeV/c^2)	R	Decay
b′	150	1.5	$b' \rightarrow tW^-$
t′	200	2.9	$t' \rightarrow b'W^+_{vir}$ $\hookrightarrow tW^-$

6.2. Hadronic Decay Modes

We start by trying the simplest possible analysis:

1. Boost the event along the z axis so that $\sum \vec{p}_z = 0$.
2. Use the thrust axis to divide the event into two hemispheres, and calculate the invariant mass of each hemisphere.
3. Plot the smaller of the two masses.

The results are shown in Figs. 22 and 23, where the latter is simply a replotting of the former with a linear scale over a more restricted mass region. It is already clear that an invariant mass cut of 104 GeV/c^2 on the least massive hemisphere has a reasonable signal to background, particularly for the t′ quark.

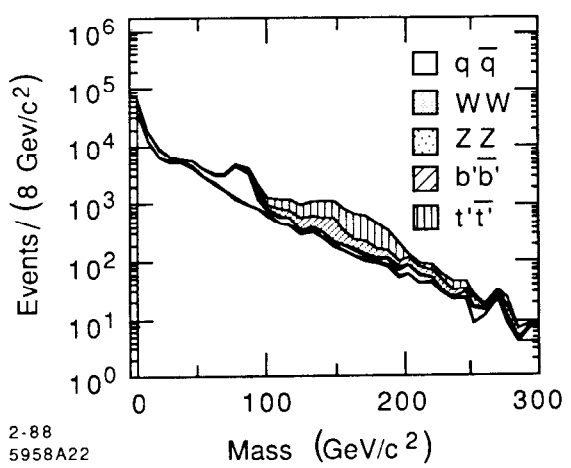

Fig. 22. The mass of the lesser mass hemisphere for t′ and b′ production and for the major backgrounds.

However, a little more sophistication is useful to clean up the signal. The signal we are looking for should have a quark jet and a W in each hemisphere. We will apply the loose constraint that this signature occurs in at least one of the hemispheres. The analysis proceeds as follows:

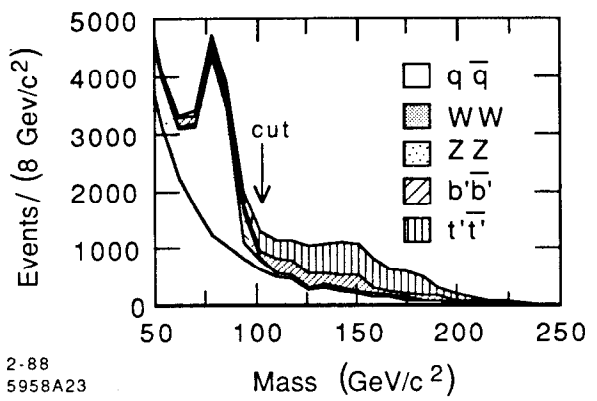

Fig. 23. The mass of the lesser mass hemisphere for t′ and b′ production and for the major backgrounds. (Same as Fig. 22 except that it is plotted on a linear scale for a restricted mass range.)

1. Perform a cluster analysis with the minimum jet separation set to 18 GeV.
2. Require a minimum of 5 clusters, with at least 2 in each hemisphere.
3. Require that in at least one hemisphere with three or more clusters the mass of two clusters is within 10 GeV/c^2 of the W mass.

The results of this analysis are shown in Fig. 24 and Table 15. Both quark states show up cleanly over the backgrounds.

There is a background that has not been included — 3 boson production: $e^+e^- \rightarrow 3Z$ and $e^+e^- \rightarrow W^+W^-Z$. These processes are presently being calculated independently by Jack Gunion and by Adrian Cooper and Mike Peskin. They are unlikely to be serious backgrounds.

6.3. Semileptonic Decay Modes

The "traditional" method of finding quarks heavier than the b is to search for isolated leptons.[17] To apply this technique, we first apply the basic analysis of the previous subsection — a cut on the smaller hemisphere mass of 104 GeV/c^2 — and additionally require an isolated lepton in one hemisphere. We

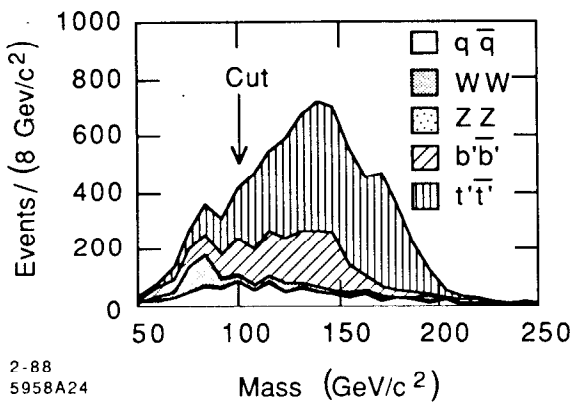

Fig. 24. The mass of the lesser mass hemisphere for t′ and b′ production and for the major backgrounds when at least one hemisphere contains two out of three jets with a mass within 10 GeV/c^2 of the W mass.

Table 15: Results for Heavy Quark Analysis Using Cluster Analysis.

	Events	Overall Efficiency	Signal/ Background
Backgrounds			
$q\bar{q}$	603	0.005	
W^+W^-	233	0.002	
ZZ	9	0.0015	
Total Background	845		
Signals			
$b'\bar{b}'$	1289	0.33	1.5
$t'\bar{t}'+ b'\bar{b}'$	5291	0.46	6.3

optimize cuts on two variables of the isolated lepton for the best signal to background ratio:

1. Lepton momentum between 5 and 100 GeV/c.

2. Isolation angle between 15° and 45°. The isolation angle is arbitrarily defined to be the half angle of a cone in which there is less than 1 GeV of additional energy.

The results of this analysis are shown in Table 16. The signal to background has improved at the cost of decreased efficiency.

Table 16: Results for Heavy Quark Analysis Using Isolated Lepton Analysis

	Events	Overall Efficiency	Signal/ Background
Backgrounds			
$q\bar{q}$	8.2	7×10^{-5}	
W^+W^-	2.4	2×10^{-2}	
ZZ	0.5	8×10^{-5}	
Total Background	11.1		
Signals			
$b'\bar{b}'$	70	0.018	6.3
$t'\bar{t}' + b'\bar{b}'$	286	0.025	19.5

7. Heavy Charged Leptons

We will now turn to the detection of a heavy charged lepton. This problem is useful, not only in its own right, but because it will lead us directly to the search for neutral Higgs bosons. It is also a process that is difficult to detect in a hadron collider.[18] For this exercise we have assumed a lepton mass of 250 GeV/c^2. After accounting for beamstrahlung and radiative effects, the effective R value is 2.3 at 1 TeV center-of-mass energy. The lepton, which we will label L, has only one decay mode:

$$L^- \rightarrow W^- \nu_L. \tag{20}$$

Thus, the production of a L^+L^- pair will yield the final state of two W's and

2ν's. One of the main backgrounds to L^+L^- production will thus be W^+W^- production, which differs only by the absence of the extra neutrinos.

As in the case of heavy quark production, there are two methods by which we could consider detecting the L^+L^- pair: the case in which both W's decay hadronicly or the case in which one W decays hadronicly and the other leptonicly. These cases are illustrated in Fig. 25.

With $E_{c.m.}$ and $p_{z_{c.m.}}$ unknown, case (d) in Fig. 25, W^+W^- pair production in which one W decays leptonicly, is a 0-C fit. Therefore, in general, case (b) in Fig. 25, L^+L^- pair production in which one L decays leptonicly will also fit it. This makes background suppression very difficult in the case in which there is a leptonic decay. Rick Van Kooten has analyzed this case and it turns out not to be completely hopeless. However the case in which both W's decay to hadrons is much superior and we will only consider that case here.

There are two additional backgrounds, illustrated in Fig. 26, which we have to consider. The first is WW-fusion production of W pairs [Fig. 26(a)]. This process, which has been calculated by Gunion and Tofighi-Niaki,[19] is an irreducible background because it leads to the identical final state as L^+L^- production. Fortunately its cross section is small, about 6% of the L^+L^- production cross section, and it peaks at lower WW invariant mass.

The second background [Fig. 26(b)] is the production of a WZ pair from γW fusion. This background was discussed at the La Thuile workshop.[15] This is an insidious background for the following reasons:

1. Since one lepton couples to a γ, it develops no appreciable transverse momentum and escapes undetected down the beam pipe.
2. Since the other lepton couples to a W, the resulting neutrino carries away transverse momentum of order the W mass.
3. The cross section is large, of order the point cross section, perhaps half of the L-pair production cross section.

In other words, the $\gamma\gamma$-fusion and WW-fusion processes are relatively benign, the former because it does not develop missing transverse momentum and the

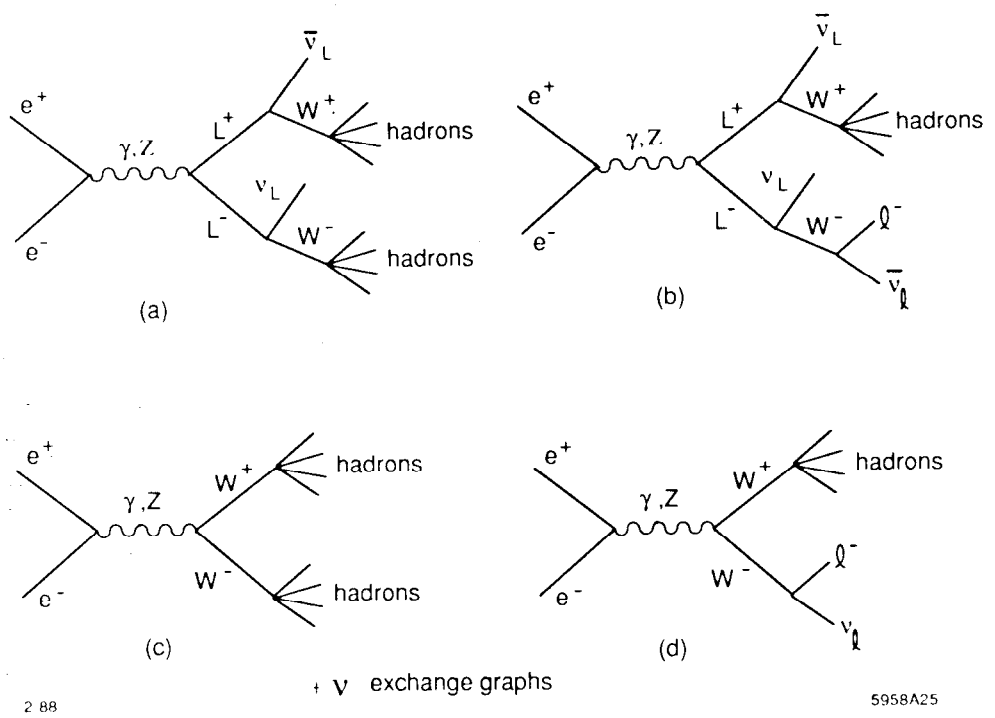

Fig. 25. Diagrams for an L^+L^- pair (a) in which both W's decay hadronicly and (b) in which one W decays hadronicly and the other decays leptonicly, and (c) and (d) for similar cases for W^+W^- pair production.

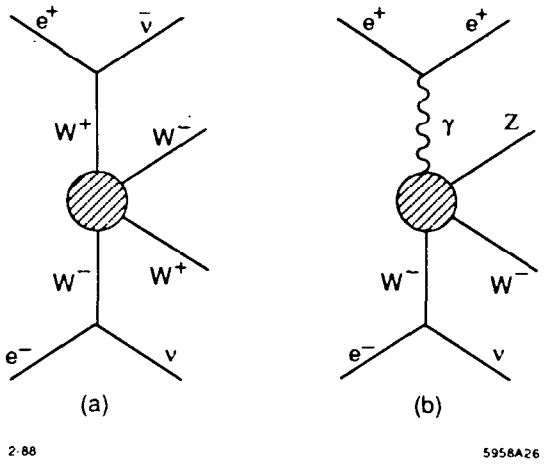

Fig. 26. (a) WW fusion and (b) γW fusion diagrams. The scattered e^+ in (b) in general goes forward and is not detected. The shaded areas represent the sum of all gauge-invariant couplings.

latter because the cross section is small. The γW-fusion process has the worst features of both — it is relatively large and it does develop missing transverse momentum. This background also suggests another class of backgrounds that need investigation: $e^+e^- \rightarrow e^\pm \nu q\bar{q}'$.

There are, however, three mitigating factors to consider concerning the γW-fusion production of WZ background:

1. The mass of the W is not equal to the mass of the Z. Our normal mass cuts will reduce the background by a factor of two.

2. The WZ system has an odd rather than even number of charged tracks. As we discussed previously, a good tracking system will gain a large factor in background suppression.

3. The process is completely calculable (and measurable with lower statistics) and can be subtracted with high precision.

We will not consider the γW-fusion background further here, but it is clear that it will have to be included in future, more detailed studies.

The analysis of L^+L^- detection follows closely the simple analysis that we did for W^+W^- detection in Section 5. The first three steps are identical, only the last discriminates between W and L pair production:

1. Lorentz transform the event along the direction of the incident beams (z-axis) so that $\sum \vec{p}_z = 0$, where the sum is over the visible charged and neutral particles.
2. Divide the event into two hemispheres using the thrust axis and require that $|\cos\theta_{thrust}| < 0.8$.
3. Require that the invariant mass in each hemisphere is within 10 GeV/c^2 of the W mass.
4. Require that the acoplanarity angle between the sum of the momenta in each hemisphere to be greater than 10°.

The results of this analysis are shown in Table 17. The largest background comes from irreducible WW fusion process. The other backgrounds are negligible. The invariant mass spectrum of the W pairs is shown in Fig. 27 along with that from WW fusion.

Table 17: Results for Heavy Lepton Analysis

	Events	Overall Efficiency	Signal/ Background
Backgrounds			
$q\bar{q}$	2	2×10^{-5}	
W^+W^-	13	13×10^{-5}	
ZZ	1	16×10^{-5}	
ZZ	41	0.11	
Total Background	57		
Signal			
L^+L^-	680	0.11	11.9

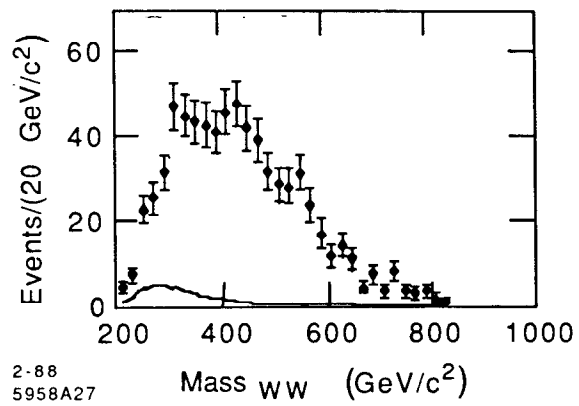

Fig. 27. The invariant mass spectrum of detected W^+W^- pairs from L^+L^- production (data points). The solid curve represents the spectrum from W^+W^- production by WW fusion.

8. Standard Higgs

8.1. Introduction

The outstanding missing piece of the standard model is the origin of the spontaneous breaking of gauge symmetry. The search for this missing piece should be the primary concern of all high-energy colliders.

The simplest way the standard model can be made consistent is by the addition of a single neutral Higgs boson. There are two major ways of producing this minimal Higgs boson in e^+e^- collisions, by annihilation into ZH and by WW fusion. Diagrams for these processes are shown in Fig. 28.

The ZH mode will be used on the Z at the SLC and LEP (with the first Z real and the second Z virtual) and at LEP II (with the first Z virtual and the second Z real). Pat Burchat has analyzed this mode for the TLC. It can be used as a verification, but the WW-fusion process is always superior at high energy. The cross section dependence, taken from a paper by Altarelli, Mele, and Pitolli[20] is shown in Fig. 29. At 1 TeV, the cross section for the WW-fusion process is 20 times larger than the annihilation process.

Higgs detection via WW fusion can be divided into two cases:

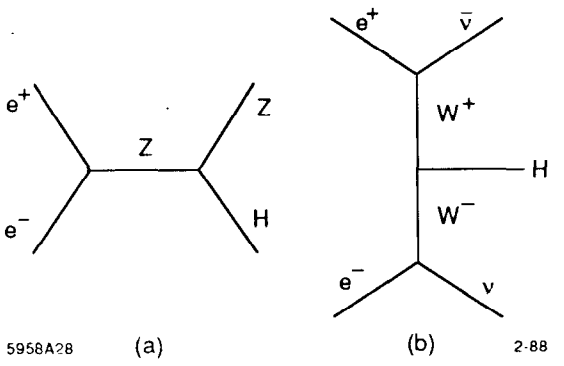

Fig. 28. Diagrams for Higgs boson production in e^+e^- collisions: (a) ZH production by annihilation and (b) H production by WW fusion.

1. $m_H \gg 2m_W$. In this case $H \rightarrow W^+W^-$or ZZ, with the bosons well separated.

2. $m_H \lesssim 2m_W$. In this case $H \rightarrow W^+W^-$ with the W's not well separated or $H \rightarrow t\bar{t}$ or $b\bar{b}$, depending on what is kinematically allowed.

We will consider these two cases separately.

8.2. High-Mass Higgs Boson

The final state is either $W^+W^-\nu\bar{\nu}$ or $ZZ\nu\bar{\nu}$. Note that this is the analysis we have just done for the case of L^+L^- production. The only thing we have to change is to expand the mass cut to have the hemisphere masses be either within 10 GeV/c^2 of the W mass or the Z mass. Looking forward to this analysis, I took the liberty of making this expansion already in Fig. 27. (It made no difference because there was essentially no background.)

To make this problem a little more challenging, we will show the results for various mass Higgs bosons on top of a background from a heavy lepton. Fig. 30 shows the results for 300, 400, and 500 GeV/c^2 Higgs bosons. In the 300 and 400 GeV/c^2 cases, the Higgs stands out easily over the heavy lepton background. It gets lost in this background when its mass reaches 500 GeV/c^2, but stands out well if there is no heavy lepton background [Fig. 30(d)]. The

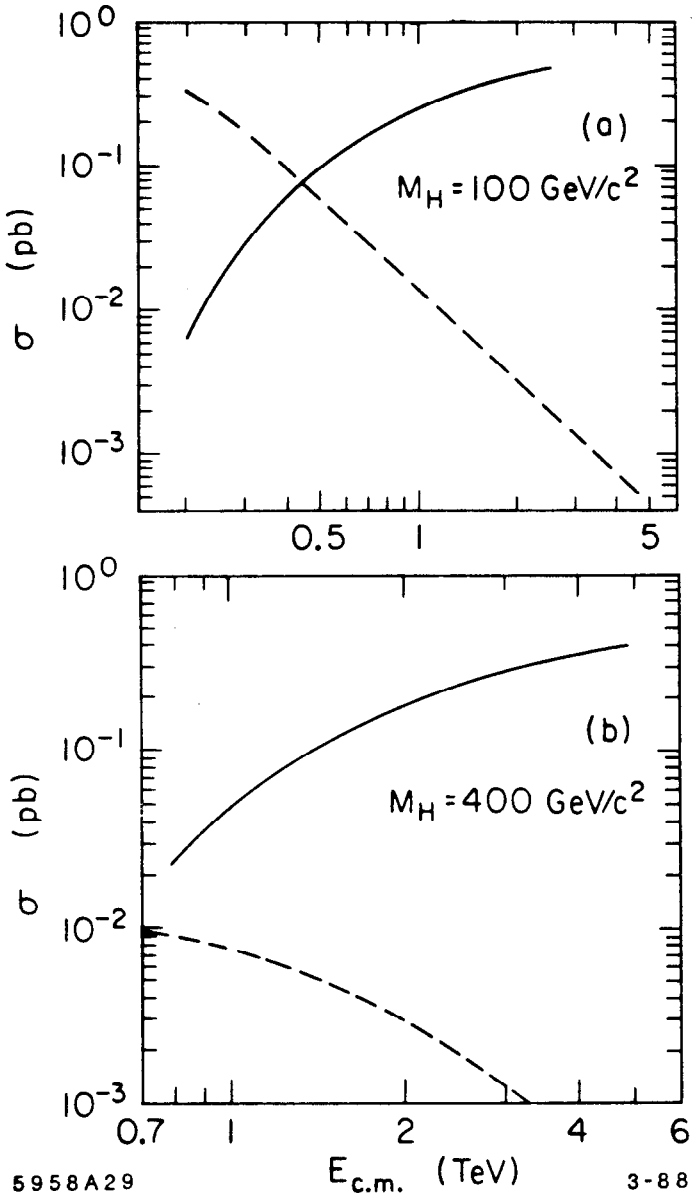

Fig. 29. Cross sections for (a) 100 GeV/c^2 and (b) 400 GeV/c^2 Higgs boson production in e^+e^- collisions. The solid curve represents the WW-fusion process, $e^+e^- \rightarrow W^+W^-\nu\bar{\nu}$, and the dashed curve represents the annihilation process, $e^+e^- \rightarrow ZH$.

$W^+W^-\nu\bar{\nu}$ production shown by the solid line in Fig. 30 can be thought of as the non-resonant WW scattering, or alternatively, as the mass spectrum of a Higgs boson with infinite mass.

The upper limit of detectability of a minimal Higgs with our assumed 30 fb^{-1} of data is probably about 500 or 600 GeV/c^2. Figure 31 shows the number of detected events and the width of the Higgs. The width increases as the cube of the mass, making the detection of masses above 600 GeV/c^2 rather difficult.

8.3. Intermediate-Mass Higgs Boson

This case is particularly interesting because it is a rather difficult, and in some cases impossible, problem in hadron colliders. We will see that it causes no difficulty in a e^+e^- collider.

The analysis can proceed in much the same way as in the high-mass case, except that the requirement that $m_{jet} = m_W$ can no longer be made. There are also some additional backgrounds that must be considered in some mass ranges.

The process of Z production by WW fusion, $e^+e^- \rightarrow Z\nu\bar{\nu}$, which is shown in Fig. 32, has been calculated by Mike Peskin. The cross section for this process is three times larger than that for Higgs production at the same mass. Thus for $m_H \approx m_Z$, the best way to find the Higgs is to measure that these "Z's" have $b\bar{b}$ branching fractions twice normal or $t\bar{t}$ branching fractions several times normal.

There are also additional insidious γW-fusion processes, as shown in Fig. 33. The single W production diagram has an enormous cross section, 136 units of R.[21] As we have mentioned previously, these backgrounds can be suppressed experimentally by noting that an odd number of charged particles have been detected.

The analysis for intermediate-mass Higgs bosons was done by Dave Burke. It has the same spirit of the analyses we have looked at so far, but varies in some details. The steps of the analysis are

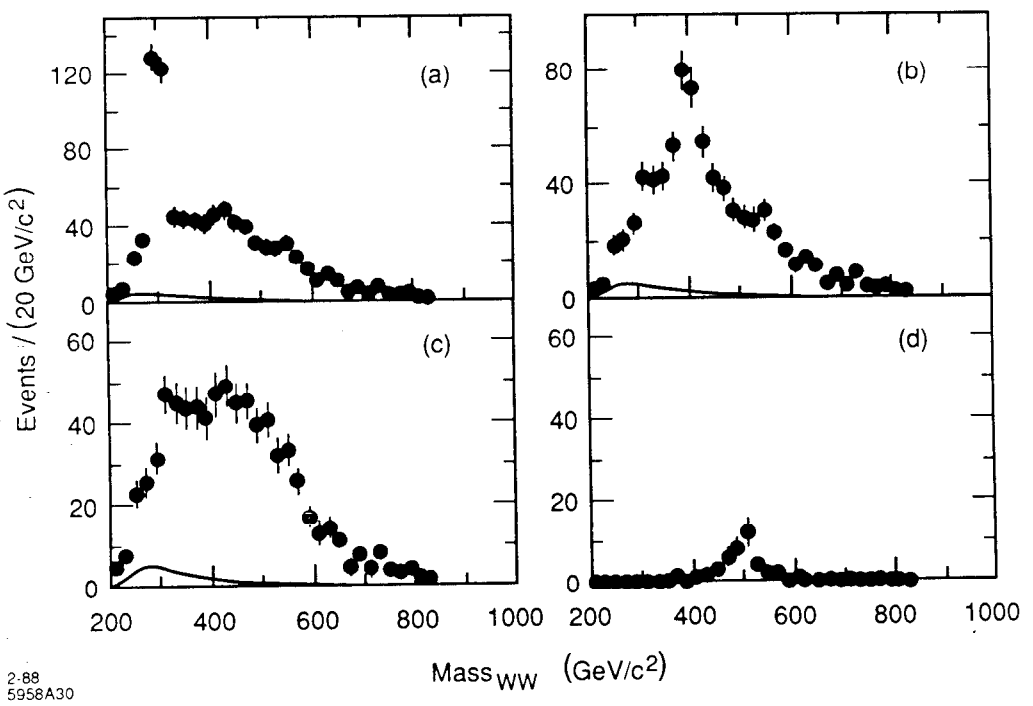

Fig. 30. The invariant mass of detected W^+W^- pairs from the sum of a 250 GeV/c^2 heavy lepton and a (a) 300 GeV/c^2, (b) 400 GeV/c^2, or (c) 500 GeV/c^2 neutral Higgs boson. (d) shows just the contribution of the 500 GeV/c^2 Higgs. The solid line represents the non-resonant W^+W^- production by WW fusion.

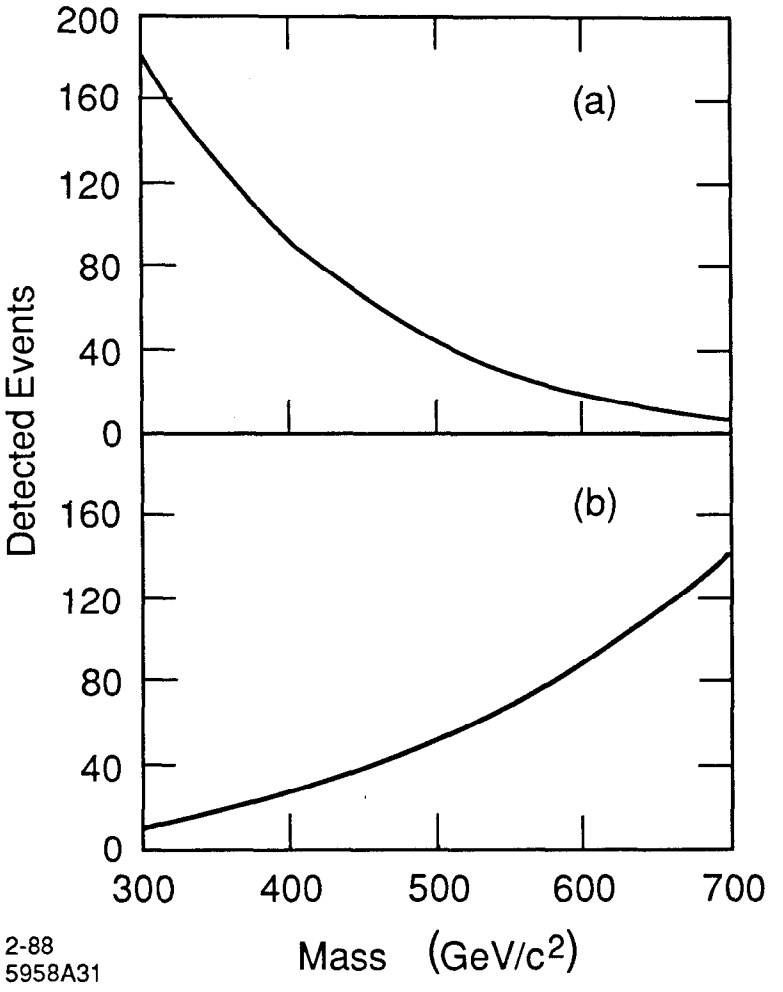

Fig. 31. (a) Number of detected Higgs bosons in 30 fb^{-1} at 1 TeV center-of-mass energy as a function of the mass of the Higgs. (b) The width of the minimal Higgs boson as a function of its mass.

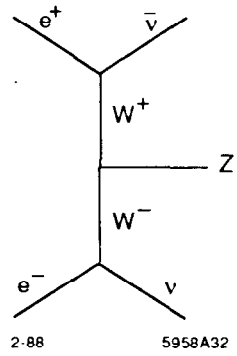

Fig. 32. Diagram for Z production by WW fusion.

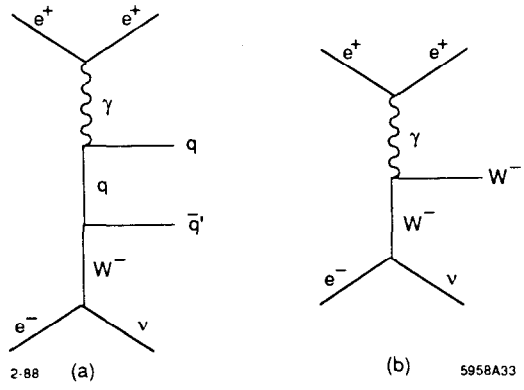

Fig. 33. Diagrams for (a) $q\bar{q}'$ and (b) single W production by γW fusion.

1. Force the cluster finder to find two jets.
2. For both jets require that $|\cos\theta_j| < 0.7$, where θ_j is the angle between the beam direction and the jet axis.
3. Require that the missing transverse momentum in the event lie between 50 and 150 GeV/c.
4. Require that there be no isolated leptons in the event.
5. Require each jet to satisfy a mass constraint appropriate to the Higgs mass being searched for.

Figure 34 shows the results for 200 and 150 GeV/c^2 Higgs bosons. In the former case the Higgs decays primarily to W pairs, but the decay products of the W's do not separate spatially because the W have little momentum. In this case the appropriate mass constraint is that $m_{jet} > 20$ GeV/c^2. In the latter case, the Higgs is assumed to decay into a $t\bar{t}$ pair with the top quark mass set at 50 GeV/c^2. In this case, the appropriate mass constraint is that m_{jet} lie between 30 and 70 GeV/c^2. In both cases, there is little background from other sources.

Figure 35 shows the cases of 50 and 120 GeV/c^2 Higgs bosons. In these cases the Higgs bosons are assumed to decay into $b\bar{b}$ pairs. The appropriate mass constraint here is that $m_{jet} < 40$ GeV/c^2. The third peak in Fig. 35 is from WW-fusion production of a single Z.

9. Charged Higgs Bosons

Charged Higgs bosons will be produced in any extension of the minimal Higgs sector. They, or something very much like them, are required in any model that tries to avoid the unnaturalness of the minimal standard model.

Charged Higgs bosons are pair produced with a cross section

$$\sigma \approx \frac{1}{3}\beta^3\sigma_{pt}. \tag{21}$$

They have the curious property of not coupling to vector bosons at the tree level — an H^+W^-Z coupling does not occur in the standard lagrangian. Thus, the normal decay of a high-mass Higgs is to the highest mass quarks: $H^+ \rightarrow t\bar{b}$. It is this property that makes the charged Higgs undetectable at hadron colliders.[22]

The analysis, which is the most complicated one that we have had to discuss, was done by Sachio Komamiya. The steps are as follows:

1. Require that the visible energy is greater than 70% of the center of mass energy.

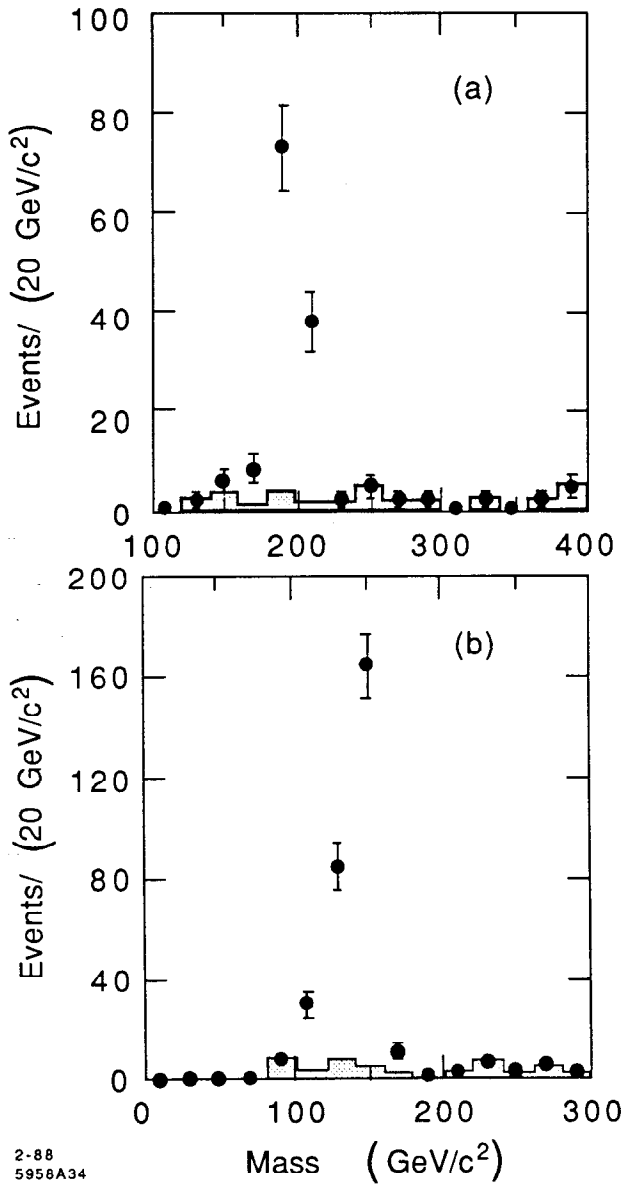

Fig. 34. The invariant mass of detected particles for the case of a (a) 200 GeV/c^2 Higgs boson that decays into vector bosons and a (b) 150 GeV/c^2 Higgs boson that decays into 50 GeV/c^2 top quark pairs. The histogram represents backgrounds from all sources except γW-fusion. In (a) each jet was required to have a mass greater than 20 GeV/c^2 and in (b) each jet was required to have a mass between 30 and 70 GeV/c^2.

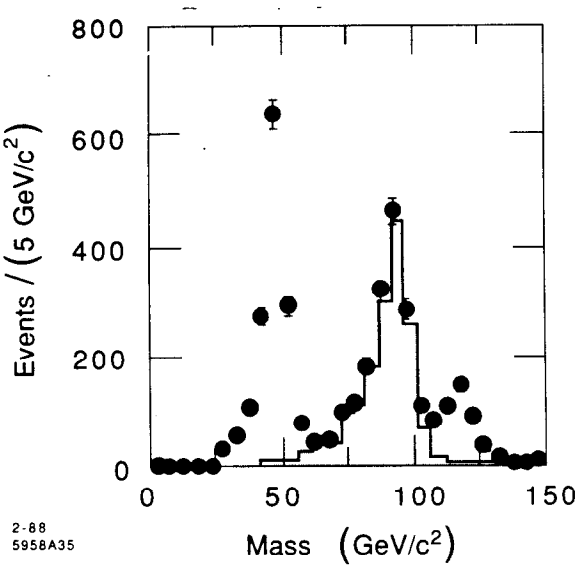

Fig. 35. The invariant mass of detected particles for the cases of 50 and 120 GeV/c^2 Higgs bosons, which are assumed to decay into $b\bar{b}$ pairs. Each jet was required to have a mass less than 40 GeV/c^2. The histogram represents backgrounds from all sources except γW-fusion. The peak at the Z mass is due to WW-fusion production of a single Z. between 30 and 70 GeV/c^2.

2. Force the cluster finder to find four jets.

3. Choose which of the three combinations of jet pairings to use by minimizing a χ^2:

$$\chi^2 = \left(\frac{\frac{1}{2}E_{c.m.} - E_i - E_j}{\frac{1}{2}E_{c.m.}}\right)^2 + \frac{1}{4}\left[\left(\frac{m_{ij} - m_H}{m_H}\right)^2 + \left(\frac{m_{kl} - m_H}{m_H}\right)^2\right], \quad (22)$$

where E_i are the jet energies that have been rescaled so that their sum equals $E_{c.m.}$, and m_H is a scanned parameter.

4. Require the following quality cuts:

   (a) $E_i > 30$ GeV for all i,

   (b) $|m_{H^+} - m_{H^-}| < 40$ GeV/c^2,

(c) $|E_{H^+} - E_{H^-}| < 20$ GeV, and

(d) $\psi_{ij} > 50°$, where ψ_{ij} is the angle between any two jets. This last requirement is tuned slightly for different Higgs mass ranges.

5. Require that there be at least three particles with $p > 1$ GeV/c and $0.2 < \delta < 2$ mm, where δ is the transverse distance of closest approach to the interaction point.

There are a couple of things to note about this analysis:

1. Unlike all of the other analyses, there is an attempt here to use all four energy-momentum constraints by requiring that the visible energy be approximately equal to the center-of-mass energy. Note however, that this is only used to choose the correct pairing of jets.

2. The final requirement reduces the background substantially. The reason is that there are four (long-lived) b quark decays in each signal event and normally at most two b quark decays in each background event.

Fig. 36 shows the resulting signals and backgrounds for 120, 200, and 300 GeV/c^2 charged Higgs bosons. In all cases, the signal easily dominates the background.

Figure 37 shows the rate of detected charged Higgs pairs for our standard run of 30 fb^{-1} of luminosity at 1 TeV. The limit of sensitivity is at a mass of about 400 GeV/c^2.

10. Conclusions

We will start with the easy issues and then move on to the harder ones.

10.1. Detector Requirements

High caliber calorimetry and tracking are required, but these are well within the state of the art. We can live with a 10° insensitive region in the forward directions, if necessary.

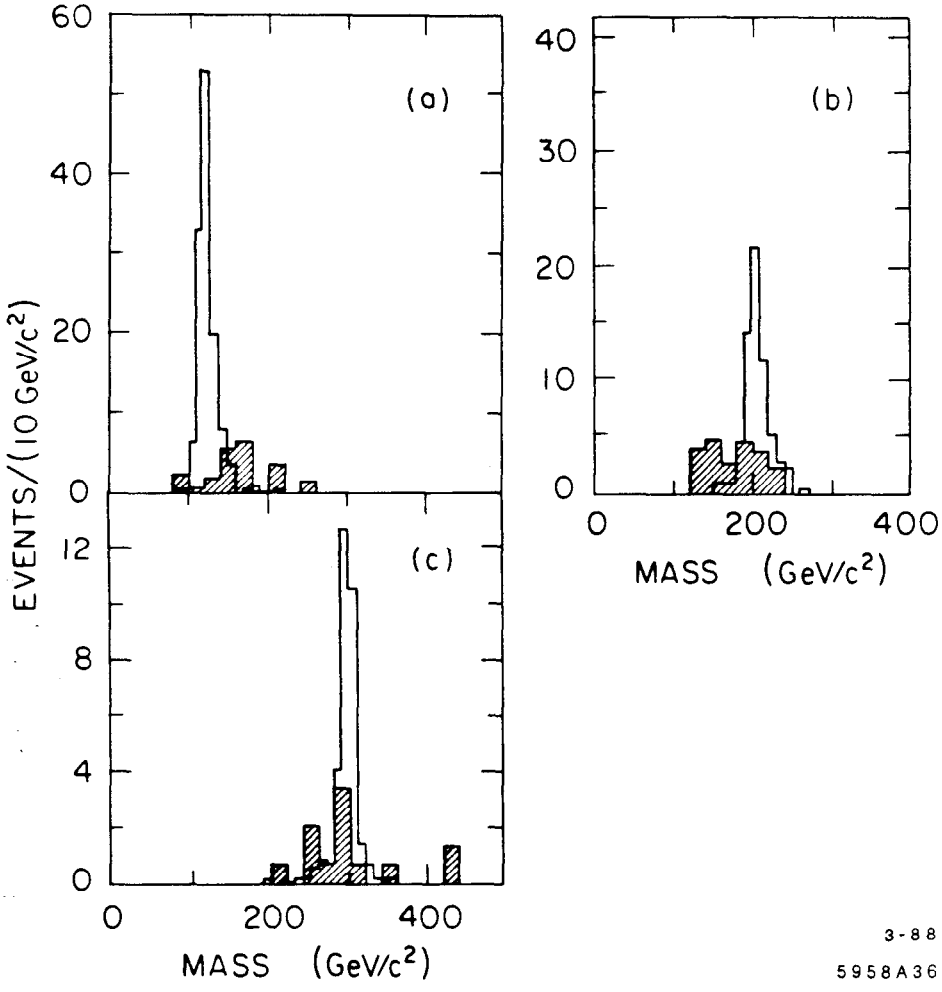

Fig. 36. Signal and background (shaded) for (a) 120, (b) 200, and (c) 300 GeV/c^2 charged Higgs bosons. Case (a) was run for 10 fb^{-1} of luminosity at $E_{c.m.} = 600$ GeV, which scales to 23 fb^{-1} of luminosity at $E_{c.m.} = 1$ TeV; case (b) was run for 10 fb^{-1} of luminosity at $E_{c.m.} = 600$ GeV, which scales to 15 fb^{-1} of luminosity at $E_{c.m.} = 1$ TeV; and case (c) was run for 10 fb^{-1} of luminosity at $E_{c.m.} = 1$ TeV.

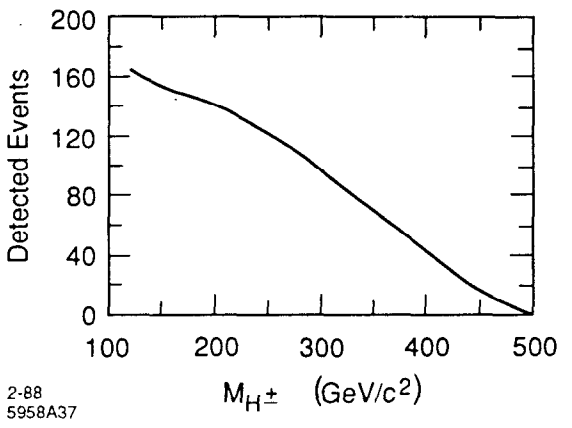

Fig. 37. Number of detected charged Higgs boson pairs in 30 fb^{-1} at 1 TeV center-of-mass energy as a function of the mass of the Higgs.

10.2. Polarization

Longitudinally polarized electron beams will be useful and are not excluded by present designs.

10.3. Beamstrahlung

Average energy losses of up to 30% are acceptable. Even higher values of δ might be acceptable but would start cutting into the effective luminosity.

10.4. Energy

The lowest energy that is reasonable to think of is three times the energy of LEP II or 600 GeV. The highest energy that anyone has discussed for the TLC is 1 TeV. It is worthwhile to compare these two options with particular attention to Higgs production.

Figure 38 shows the threshold factors for different types of reactions with and without the effect of beamstrahlung. The figure requires a bit of explanation. The horizontal axis gives the energy in units of the threshold of the reaction in question. For example, if the threshold is 400 GeV (*i.e.*, a 200

GeV/c^2 charged Higgs pair or a 400GeV/c^2 neutral Higgs), then a 600 GeV collider would appear at 1.5 and a 1 TeV collider would appear at 2.5. Thus the cross section for a charged Higgs pair (curve labeled "Axial/scalar") is about the same at the two energies, but the cross section for a neutral Higgs (curve labeled "Fusion") is about an order of magnitude higher at 1 TeV as at 600 GeV. This is made more explicit in Fig. 39, where the gain in the number of events for 1 TeV compared to 600 GeV is plotted versus the threshold mass.

Figure 40 shows the number of detected events for the two different energy colliders for single Higgs production as a function of Higgs mass for our standard assumption of 30 fb^{-1} of integrated luminosity. The discovery limit in both cases is about half the center-of-mass energy.

Table 18 gives the discovery limits for 30 fb^{-1} of integrated luminosity for all of the processes that we have discussed. The limits all turn out to scale approximately linearly with the energy. There is no way to give a strong argument for any particular energy since we do not know the scale of new physics. However, since the vacuum expectation value of the Higgs field is 246 GeV, the gain in discovery limits by going to 1 TeV seems like a good bet.

Table 18: Discovery Limits for 30 fb^{-1} of Data

Process	$E_{c.m.}$ in GeV 600	1000
Z′	600	1000
Heavy quarks and leptons	~300	~500
Standard Higgs	300	500
Charged Higgs	240	400

10.5. Luminosity

The value we have been using as a test value, 30 fb^{-1}, seems well matched to getting the maximum discovery range for Higgs events independent of energy.

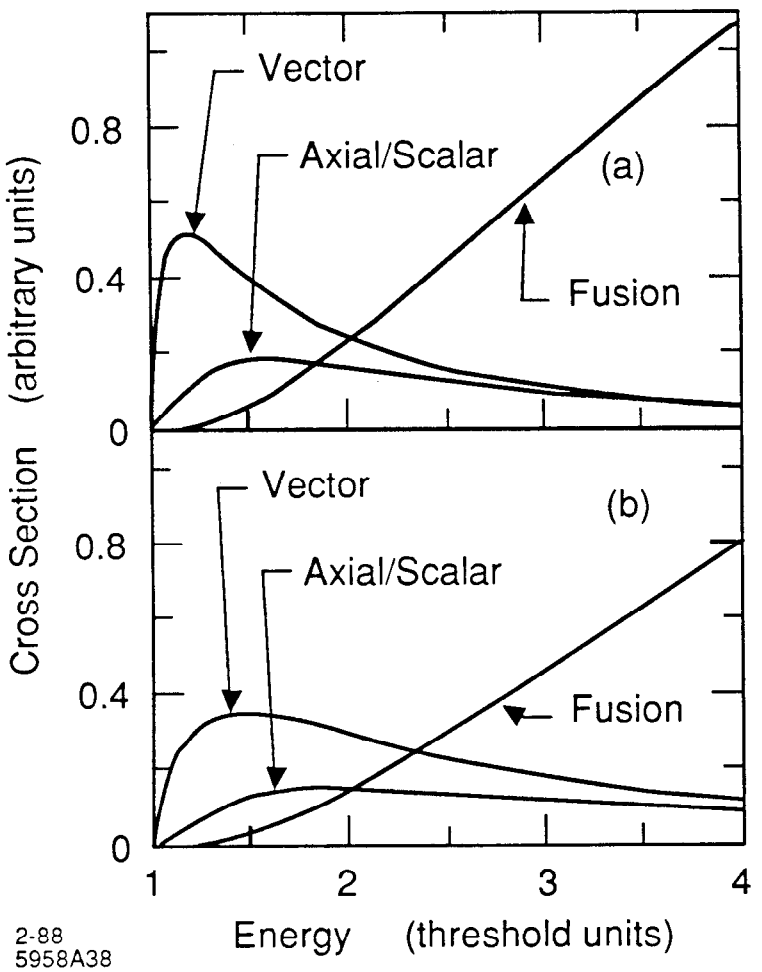

Fig. 38. The relative cross sections versus energy expressed in threshold units (a) without and (b) with beamstrahlung for fermions pair produced by a vector current, fermions pair produced by an axial current or pair produced scalars, and for particles produced by the fusion process. See text for an example.

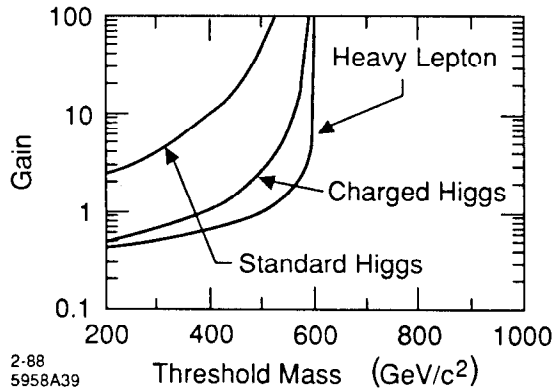

Fig. 39. The gain in number of events for fixed integrated luminosity of a 1 TeV collider over a 600 GeV collider for different processes as a function of threshold mass.

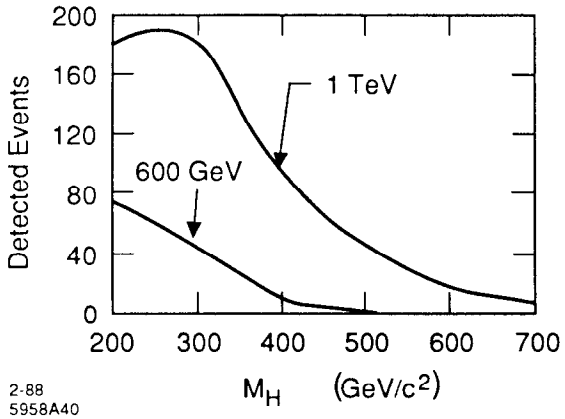

Fig. 40. The number of detected single Higgs events for a 600 GeV and a 1 TeV collider for 30 fb^{-1} of integrated luminosity as a function of Higgs boson mass.

It is not necessary to get this amount of integrated luminosity in one year. Five years is probably a reasonable time integral to consider for this initial block of luminosity.

The question we have to consider is: What is a realistic derating factor between design luminosity and actual integrated luminosity? It must be realistic because these is not much headroom at the TLC. For example, we talk of getting millions of Z's at the SLC, but in fact most of the hypothetical discoveries could be made with only 10,000 events. With the sole exception of a Z' resonance, this large margin for error does not exist at the TLC.

To make this discussion quantitative, let me define the "design second." This is a unit of integrated luminosity equal to that which would be obtained in one second at design luminosity. Thus, the design luminosity of the TLC should be given by

$$\mathcal{L}_{design} = \frac{3 \times 10^{40}\ \mathrm{cm}^{-2}\mathrm{sec}^{-1}}{\text{number of design seconds in 5 years}}. \tag{23}$$

How many design seconds are there in five years? For storage rings, PEP is a good example. It had a design luminosity[23] of 10^{32} $\mathrm{cm}^{-2}\mathrm{sec}^{-1}$ and it ran for about five years between turn-on and the temporary turn-off for SLC commissioning. The most integrated luminosity any experiment collected was 300 pb^{-1}. Thus, for PEP, there were 3×10^6 design seconds in 5 years, or 35 design days.

Although this value does not seem exemplary, PEP is one of the more favorable cases that we might have picked. The only better case I know of for e^+e^- storage rings is CESR at Cornell. It was about a factor of two better in its first five years and now, after eight years of operation, it is actually running above its original design luminosity. On good days, it approaches one design day per calendar day.

If we simply plug the PEP value into Eq. (23), we obtain

$$\mathcal{L}_{design} = 1 \times 10^{34}\ \mathrm{cm}^{-2}\mathrm{sec}^{-1}. \tag{24}$$

Of course, the TLC is not a storage ring, and this might not be the right number. It would be better to use the SLC as a guide. There are two counter-balancing arguments that might be put forward:

1. The SLC case is too pessimistic because we will learn from our mistakes.
2. The SLC case is too optimistic because the TLC is a much more difficult machine.

Both of these arguments are clearly valid.

This design luminosity is an order of magnitude higher than that shown in Table 9. However, we should not be discouraged at this point because we have not yet pulled all of the rabbits out of the hat. Table 9 is for a single bunch machine. Higher luminosity can be achieved without using much more power by considering multi-bunch operation.

11. Prospects

We have seen in these lectures that the physics of e^+e^- linear colliders is extremely attractive. These colliders will fill crucial holes in the physics capabilities of hadron colliders, and they will allow a more detailed study of the effects that may be seen in hadron colliders.

The technical design work is at a very early stage. We should see a great deal of progress and a convergence of views as research and development progresses over the next few years.

Linear colliders clearly have an important role in the future of particle physics; we should vigorously pursue planning, research, and development on them.

References

1. M. E. Peskin, these proceedings.
2. B. Richter, *Nucl. Instrum. Methods* **136**, 47 (1976).
3. Advisory Panel on the Prospects for e^+e^- Linear Colliders in the TeV Range, CERN report number CLIC note 38 (May, 1987) and K. Johnsen in the *Proceedings of the Workshop on Physics at Future Accelerators,* La Thuile, Italy and Geneva, Switzerland, January 1987, CERN report number CERN-87-07 (1987). There are some detailed differences between these two reports. I have tried to take a consistent set of parameters.
4. The SLAC collider design does not have an official name, but we have to call it something. Mike Peskin gets credit for coming up with TLC.
5. Throughout these lectures the design parameters of the SLC will be used although some of the design parameters such as the 180 Hz repetition rate may never be achieved due to fiscal constraints.
6. Useful discussions of the interdependence of parameters for linear colliders include P. B. Wilson, SLAC report numbers SLAC-PUB-3674(Rev.) (1985) and SLAC-PUB-3985 (1986), J. R. Rees, SLAC report number SLAC-PUB-4073 (1986), and R. Palmer, SLAC report number SLAC-PUB-4295 (1987).
7. R. Hollebeek, *Nucl. Instrum. Methods* **184**, 333 (1981). For more recent work see P. Chen and K. Yokoya, SLAC report number SLAC-PUB-4339 (1987)
8. R. Hollebeek and A. Minten, SLAC report number CN-302 (1985).
9. J. R. Rees claims responsibility for this unfortunate coinage.
10. R. J. Noble, *Nucl. Instrum. Methods* **A256**, 427 (1987); R. Palmer, SLAC report number AAS Note 30 (1987). See also P. Chen, SLAC report number SLAC-PUB-4379 (1987).
11. See, for example, C. Dib and F. J. Gilman, *Phys. Rev. D* **36**, 1337 (1987).

12. D. Blockus *el al.*, "Proposal for Polarization at the SLC," SLAC report number SLAC-PROPOSAL-SLC-01 (1986)

13. SLD Design Report, SLAC report number 273 (1984).

14. R. Wigmans, NIKHEF report number NIKHEF-H/87-12 (1987).

15. D. Froidevaux in the *Proceedings of the Workshop on Physics at Future Accelerators,* La Thuile, Italy and Geneva, Switzerland, January 1987, CERN report number CERN-87-07 (1987).

16. J. Dorfan and R. Van Kooten, SLAC report number SLAC-PUB-4334 (1987).

17. G. Hanson in *Proceedings of the Third Mark II Workshop on SLC Physics,* Pajaro Dunes, February 25-28, 1987, SLAC report number SLAC 315 (1987).

18. V. Barger, T. Han, and J. Ohnemus, University of Wisconsin report number MAD/PH/331 (1987), but see also Ref. 15.

19. J. F. Gunion and A. Tofighi-Niaki, *Phys. Rev. D* **36**, 2671 (1987).

20. G. Altarelli, B. Mele, and F. Pitolli, *Nucl. Phys.* **B287**, 205 (1987).

21. E. Gabrielli in the *Proceedings of the Workshop on Physics at Future Accelerators,* La Thuile, Italy and Geneva, Switzerland, January 1987, CERN report number CERN-87-07 (1987).

22. H.-U. Bengtsson, H. Yamamoto, and S. Komamiya, SLAC report number SLAC-PUB-4369 (1987).

23. PEP Conceptual Design Report, SLAC report number SLAC-189 (1976).